Discrete Proton Arc Therapy for Neuro-Oncological Patients:

Feasibility and Plan Comparison with IMPT

BM51035: BME MSc-thesis
Pelagia Fotiadou

Delft University of Technology

TUDelft

Discrete Proton Arc Therapy for Neuro-Oncological Patients:

Feasibility and Plan Comparison with IMPT

by

Pelagia Fotiadou

Student Number: 5719976
21 January 2025

Thesis in Partial Fulfillment of the Requirements for the Degree of Master of Science in

Biomedical Engineering

Delft University of Technology; HollandPTC

Supervisors: Prof. Dr. Danny Lathouwers, TU Delft
Dr. Steven Habraken, HollandPTC
Dr. Jasper Kouwenberg, HollandPTC
RTT. Koen Crama, HollandPTC

Thesis committee members: Prof. Dr. Danny Lathouwers, TU Delft (chair)
Dr. Steven Habraken, HollandPTC
Prof. Dr. Mischa Hoogeman, TU Delft

TUDelft

Acknowledgements

Contents

Nomenclature

AA   Anaplastic Astrocytoma

CNS   Central Nervous System

CT   Computed Tomography

CTV   Clinical Target Volume

DSB   Double Strand Break

DT   Delivery Time

ELST Energy Layer Switching Time

ESS   Energy Selection System

HU   Hounsfield Units

IMPT Intensity Modulated Proton Therapy

IQR   InterQuartile Range

LET   Linear Energy Transfer

LVH   LET Volume Histogram

MC   Monte Carlo

MLC   Multi Leaf Collimator

MRI   Magnetic Resonance Imaging

MU   Monitor Unit

OAR   Organ At Risk

PAT   Proton Arc Therapy

PBS   Pencil Beam Scanning

PET   Positron Emission Tomography

PTV   Planning Target Volume

RBE   Relative Biological Effectiveness

SOBP Spread-out Bragg Peak

WHO World Health Organization

1

Introduction

From the acknowledgment of protons' therapeutic potential in 1946 to the first patient treatment in 1954 and the establishment of the first hospital-based proton facility in 1990, it's clear that proton therapy has made significant advancements [1]. The interest in adopting this modality over conventional radiotherapy stems from critical advantages, such as the favorable depth-dose characteristics of protons. For protons within the therapeutic 70-250 MeV range, the depth distribution follows the infamous Bragg-peak scheme, which results in an increased ionization density near the end of their range while delivering zero exit dose [2].

Proton Arc Therapy (PAT) is considered an advancement over traditional proton therapy because it can enhance the tumor dose distribution while offering a better protection to the surrounding Organs At Risk (OARs). Nonetheless, certain limitations need to be addressed, such as the prolonged treatment times caused by the irradiation from multiple angles combined with extended gantry rotation times, among other factors.

The project's objective is to assess the potential benefits of PAT compared to single-field, robustly optimized Intensity-Modulated Proton Therapy (IMPT), currently used as an adjuvant therapy for neuro-oncological patients following surgical resection. Neuro-oncological patients were chosen due to their heightened risk of radiation-induced toxicities following proton radiation therapy. While PAT may involve longer treatment sessions, these could be mitigated by improvements in dosimetric quality and plan robustness.

For this study, multiple PAT plans were created for each patient using the RayStation software (RaySearch Laboratories, Stockholm, Sweden). The software provides a wide range of options for designing the treatment plans, such as selecting the number of beam directions, energy layers, iterations, and more. For each of the 10 patients in the cohort, six PAT plans were generated, with the clinical plan, used for the patient's actual irradiation, serving as the reference for comparison.

The comparison between the PAT plans and the clinical plan was mainly based on three key factors: treatment time, robustness, and the distributions of the Linear Energy Transfer (LET) and Relative Biological Effectiveness (RBE).

At the end of this thesis, conclusions will be drawn regarding the potential benefits of this technique for the treatment of neuro-oncological patients. Additionally, its limitations will be addressed and discussed to provide a comprehensive conclusion.

2

Background

2.1. Brain tumors: Gliomas

Glioma is a general term for neuroepithelial tumors that arise from the glial cells in the Central Nervous System (CNS), primarily oligodendrocytes and astrocytes [3]. These tumors make up 24% of all primary brain and CNS tumors, occurring almost exclusively in the brain's four lobes. The frontal lobe has the highest occurrence rate at 23.6%, while the occipital lobe has the lowest at 2.8%. A small percentage of gliomas can also appear in the brainstem, cerebellum, and spinal cord.

According to the World Health Organization's (WHO) classification, gliomas are divided into four grades, with the first two grades being considered as low-grade gliomas and the latter two as high-grades gliomas, which typically have a poor prognosis.

- WHO Grade I: Pilocytic Astrocytoma

- WHO Grade II: Astrocytoma

- WHO Grade III: Anaplastic Astrocytoma (AA)

- WHO Grade IV: Glioblastoma Multiforme

In this project, patients with WHO Grade III AA are included. AA is a diffusely infiltrating, malignant primary brain tumor arising from the neoplastic transformation of astrocytic cells and it usually evolves into WHO Grade IV glioblastoma multiforme [4]. AA represents 6-7% of all gliomas and 1.7% of all tumors with 5-year survival of 30% and a median overall survival of 3 years.

2.1.1. Risk Factors

Several risk factors for gliomas are widely recognized, such as genetic predisposition, exposure to ionizing radiation, and a history of allergies. However, many tumors develop without these known exposures or genetic conditions, indicating the need for further research to establish definitive links with occupational, environmental, and lifestyle factors.

2.1.2. Symptoms and Diagnosis

Symptoms

Compared to low-grade gliomas, high-grade gliomas are typically diagnosed in individuals over the age of forty [4]. The clinical symptoms vary depending on the tumor's location and can include focal or generalized neurological deficits, headaches, visual and sensory impairments, speech disorders, and loss of strength, among others. Seizures are less common in AA than in low-grade gliomas.

Diagnosis

The gold standard for diagnosing, managing, and monitoring the treatment response is brain Magnetic Resonance Imaging (MRI) with Gadolinium contrast. In most cases, AA presents as a T1-weighted hypointense and T2-weighted hyperintense mass, often accompanied by surrounding edema and potentially enhancing nodular areas [5]. AA does not usually involve calcifications. It exhibits a homogeneous signal intensity on T2-weighted brain MRI sequences, has a well-defined margin, and generally does not invade the cerebral cortex [6].

Perfusion MRI is also used for the diagnosis of gliomas, since it offers the ability to distinguish between low-grade and high-grade forms of astrocytomas with the high-grade astrocytomas being associated to higher blood volume [7].

Positron Emission Tomography (PET) can also be a valuable tool for diagnosing and managing glioma patients. It allows for non-invasive grading of gliomas and offers a more precise diagnosis. Additionally, PET provides insights into the biological response to treatment, helps delineate the tumor volume, and assists in treatment planning.

2.1.3. Cancer Treatment Options

Surgery alone cannot be considered curative in the treatment of AA and, therefore, post-surgical treatment must always be considered. The primary treatment for these malignancies is complete resection, as it offers favorable prognostic outcomes. Radiotherapy and chemotherapy can be used as adjuvant treatments following surgery, or as primary treatments when surgery is not feasible, in case of the tumor being in close proximity with critical structures. For WHO Grade III glioma patients, the combination of chemotherapy and radiation therapy nearly doubles the median survival compared to radiation alone [8].

Chemotherapy

Chemotherapy is administered either by injection or in a pill form to destroy or inhibit the growth of cancer cells. Temozolomide is a commonly used drug in treating glioma patients. This drug sensitizes the tumor to radiation and therefore chemotherapy is usually followed by radiation for optimal treatment outcome.

Another option in the chemotherapy treatment of glioma patients is the drug Bevacizumab, used to block the growth of new blood vessels that nourish the tumor. Bevacizumad is often used after a tumor returns and is considered very effective at easing the symptoms [9].

Radiotherapy

Both photon and proton therapy have been used individually as secondary treatments for glioma patients. The main difference in the outcomes that these two options produce, lies in the interaction of the particles with the medium. Photons can indirectly damage DNA by generating secondary electrons, primarily through Compton scattering. In this process, a photon interacts with an electron that is loosely bound to an atom, transferring some of its energy to the electron, which is then ejected as a secondary electron. These secondary electrons subsequently interact with the abundant water molecules in the surrounding environment, leading to the creation of free radicals that can consequently damage the cancer cells. On the other hand, protons are causing damage to the DNA of these cells, by directly interacting with it. The principle goal of the interaction of ionizing radiation with the matter is the production of DNA Double Strand Breaks (DSBs). According to [10], DNA DSBs occur when both complementary strands of the DNA double helix are simultaneously broken at sites close enough that base pairing is insufficient to keep the two DNA ends connected. Enough accumulation of these DSBs leads cancer cells to apoptosis.

Side-effects of Radiotherapy

The radiotherapy damage to the hypothalamic-pituitary axis, the system that communicates with hormone-producing glands in the body, can lead to endocrine dysfunction affecting adrenal, gonadal, and thyroid hormones [11]. It has been observed that radiation therapy for these malignancies is frequently associated with permanent or disabling side effects, such as neurocognitive impairment, neurological deficits, neurovascular complications, neuroendocrine deficiencies, and radiation-induced cancers. However, because deficits are often subjective and may already be present before treatment, linking the effects of radiation to cognitive function is challenging [12].

2.2. Photon Therapy

2.2.1. Equipment

In photon therapy, a photon beam is created using a Linear Accelerator (LINAC). Here, high-energy electrons are generated in the LINAC's vacuum and directed at a high atomic number target. When these electrons interact with the atoms in the target, a process called Bremsstrahlung occurs, leading to the emission of photons. Bremsstrahlung occurs as an electron is slowed down and deflected by an atomic nucleus, causing its lost kinetic energy to be converted into electromagnetic radiation, in accordance with the law of conservation of energy. The produced photons are then directed towards the Multileaf Collimators (MLCs), where the beam is shaped and conformed to the shape of the tumor, ensuring efficient irradiation of the target while minimizing exposure to the surrounding healthy tissue. A schematic view of the LINAC components mentioned is given in Figure 2.1.

2.2.2. Dose-Depth Characteristics

The produced photons that are directed into the patient deposit their energy into the tissue, with the radiation dose decreasing exponentially as the depth increases, as can be seen in Figure 2.2.
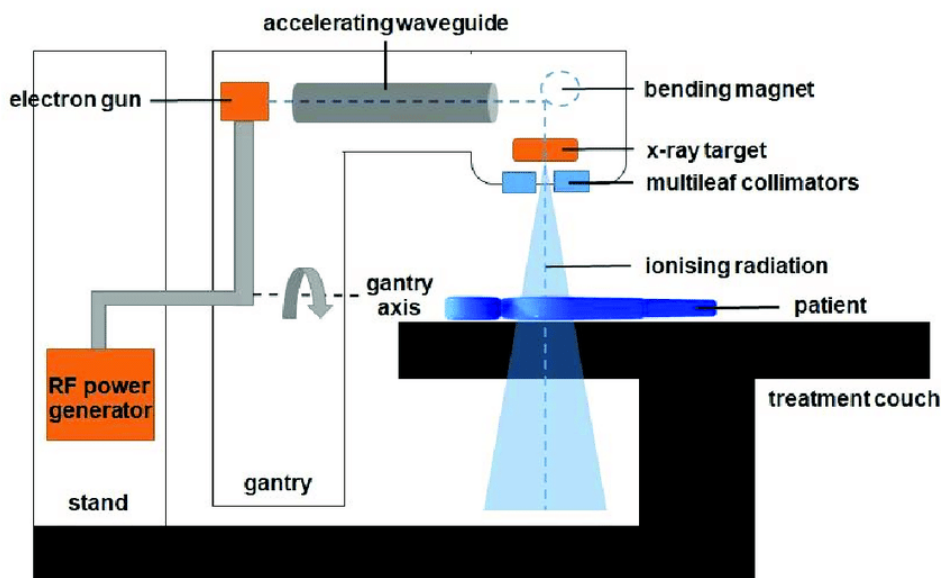
Figure 2.1: Schematic side view of a LINAC's components.

2.3. Proton Therapy

2.3.1. Equipment

In proton therapy, a proton beam is generated using a synchrotron or cyclotron, devices that accelerate charged particles. In HollandPTC, a superconducting isochronous cyclotron is used to produce the proton beam, which is subsequently directed towards the Energy Selection System (ESS) [13]. The ESS consists of three high-density graphite wedges which are positioned via a linear movement into the beam path to allow precise and fast variation of beam energy within the 70 MeV to 244 MeV energy range. A beam transport system then focuses, shapes, and guides the beam to the treatment room, creating the small beam size necessary for proton treatments and enabling the targeting of very small spots across the full energy range.

Once the proton beam is directed into the gantry room, the protons will encounter the nozzle. The nozzle consists of four steering magnets and an ionization chamber. The steering magnets are used for the scanning process and the ionization chamber for providing feedback to the treatment system to ensure accurate delivery.

Another important part of the nozzle is the range shifter, a uniform plastic slab used to treat tumors located near the surface. Although the ESS is responsible for choosing the appropriate energy level to target the tumor based on its depth, there are technical limitations that make it challenging to treat tumors situated close to the minimum range, even when the lowest proton energy is applied, making the use of a range shifter necessary. When the protons interact with the plastic material, they deposit part of their initial energy, while also leading to significant beam broadening due to the scattering effects that take place.

Although recent studies suggest that range shifters may not be needed for certain clinical cases, their use should not be completely ruled out for large superficial targets, as they can provide a more uniform dose distribution [14]. For lung and esophageal

tumors, range shifters are employed to enhance robustness against interplay effects.

2.3.2. Dose-Depth Characteristics

The interaction of protons with the tissue leads to an increased ionization density near the end of their path, known as the Bragg peak. This dose deposition pattern allows protons to deliver an increased dose to the tumor while sparing the nearby critical structures. Protons offer a superior physical dose distribution compared to photons while decreasing the integral radiation dose exposure. Proton therapy aims at reducing the radiation-induced late effects, because the Bragg peak can be precisely placed at a desired depth inside the patient's body through accurate modulation of the proton energy, while delivering zero exit dose.

Exploitation of multiple Bragg peaks is also encouraged because they can be shifted in depth and weighted to create a Spread-Out Bragg Peak (SOBP). This is considered a key feature for the delivery of homogeneous dose to tumors of significant depth.
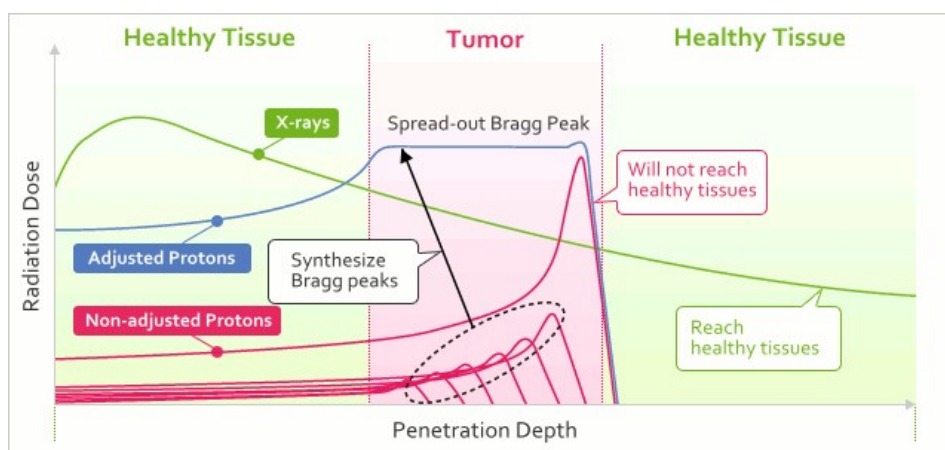
Figure 2.2: Depth dose distribution for X-rays (green line) and protons (pink line). Protons deposit only a small dose at the entrance of their path and deliver their maximum dose at a specific depth, dependent on their initial energy. By combining proton beams with various energies, an extended uniform dose region, known as the Spread-out Bragg Peak (blue line), is created [15].

There are two main methods for delivering a proton dose to a patient, namely the passive scattering and the pencil beam scanning (PBS) techniques.

2.3.3. Passive Scattering

In passive scattering, the concept of the SOBP is employed. The range of this peak is determined by the proton beam's energy, which is either selected by the accelerator system or reduced using passive materials [16]. The SOBP is created using a range modulation wheel that rotates continuously and has steps of varying thicknesses. Each subset of protons in the beam interacts with a different thickness of the wheel, resulting in different energies and penetration depths, thus forming the SOBP.

2.3.4. Pencil Beam Scanning

A proton beam, guided by magnetic fields, can be directed to various points in the plane perpendicular to the central axis of the field along arbitrary paths. Consequently, a narrow, unscattered beam, known as a pencil beam, can be targeted at any spot within the patient by controlling its position in the perpendicular plane and adjusting its energy to determine its depth [17].

There are different categories of PBS, including spot scanning that delivers the radiation in discrete spots with the beam off between the spots, raster scanning that delivers radiation to spots with the beam on between them, and line scanning that irradiates in a continuous scanning line with the beam on continuously [18].

The development of PBS paved the way for advanced proton therapy techniques, including IMPT. IMPT is a sophisticated method that employs inverse planning algorithms to fine-tune the dose distribution. In this approach, multiple pencil beams are adjusted in terms of energy and intensity to precisely match the tumor's shape. This enables IMPT to deliver highly conformal doses even to complex tumor volumes, including those with irregular shapes or those located near critical structures. The ability to modulate the fluence of the pencil beams across different areas allows IMPT to effectively spare healthy tissues while ensuring accurate coverage of the target.

2.4. Proton Arc Therapy

Another advanced proton therapy technique made possible from the development of PBS, is PAT. PAT is capable of delivering highly precise, conformal doses to tumors by rotating the nozzle around the patient and delivering the dose from multiple angles. This rotation can be achieved by using either a dynamic arc or a step-and-shoot method [18]. Before PAT dynamic is clinically feasible, the step-and-shoot method can be utilised as an alternative solution using the state of technology at existing proton therapy centers with a similar degree of freedom, at the expense of treatment efficiency in comparison to the dynamic method. PAT step-and-shoot mode is also less demanding given that it does not require a dynamic rotational gantry. It was reported that treatment plans using multiple fields provide similar dose distributions and treatment characteristics as PAT dynamic techniques, while offering better plan quality compared to IMPT [19].

One of the advantages of particle arc treatment, is that it can be used on various treatment sites and clinical scenarios due to the additional degrees of freedom that it offers in comparison to a limited number of static beams. Arc trajectories include full, partial or multiple arcs. Arc trajectory consideration may depend on the location of the tumor but also on the location of the OARs. For instance, for non-centrally located tumors, partial arcs can be used that pass only through the direction closest to the target. This approach helps minimize radiation exposure to healthy tissue while still ensuring optimal coverage of the tumor.

Another anticipated benefit of PAT is the reduction of skin doses, achieved by using multiple beam directions with fewer energy layers per direction. This approach may help mitigate the common side effect of radiation dermatitis associated with proton therapy [20]. Radiation dermatitis is mainly the result of the SOBPs. Although com-

bining Bragg peaks of various energies ensures a uniform dose across the target depth, it also raises the entrance dose due to the cumulative effect of the entrance doses from each individual monoenergetic Bragg peak.

Studies have shown that while PAT can lead to reduced isodose volumes for an increased number of beam directions, this advantage comes with the drawback of larger low-dose (< 2 Gy) volumes. As the target area is irradiated from multiple angles, the likelihood increases that one or more beams will pass through the same healthy tissue, resulting in a larger volume of tissue receiving low doses of radiation. This increase in low-dose volumes may suggest a heightened risk of secondary cancer, particularly in pediatric glioma patients whose developing brains are particularly sensitive to radiation [21]. Conversely, IMPT results in a higher dose focused on a smaller region, so selecting between these proton therapy techniques will depend on the specific considerations regarding the patient.

2.5. Treatment Planning in PAT

A crucial component in creating an ideal treatment plan is the treatment planning system. Key parameters to consider, include precise radiation dose delivery to the tumor, effective protection of the surrounding critical structures, treatment effectiveness, and patient safety. According to [18], PAT systems need to focus on four key aspects of planning: (1) delivery time (2) plan quality, including robustness, (3) computational efficiency, particularly through the optimization of the planning algorithms, and (4) LET and RBE distributions. This project will address all of these parameters except for computational efficiency.

2.5.1. Delivery Time

One of the main challenges associated with PAT is the extended duration of treatment delivery. This is caused by expanding the number of angles to create an arc and integrating multiple energy layers within each beam of the arc. The total beam delivery time is a combination of the energy layer switching time, the spot travelling time between spots of an energy layer, the dose delivery time at each spot as well as the beam switching time.

Energy Layer Switching Time

The time needed to change the energy between different layers is known as the Energy Layer Switching Time (ELST). Shifting from high to low energies is relatively slow but still quicker than the shift from low to high energies, due to a phenomenon known as magnetic hysteresis. This phenomenon causes eddy currents to form in the bending magnets during transitions between energy layers, which in turn slow the rate at which the magnetic field changes, extending the time needed for the magnetic field to stabilize [22]. Representative data regarding the time needed for energy switch ups and downs may vary from hardware to hardware but typical values are 5.5 s and 0.7 s respectively [23]. For the Varian ProBeam system that is utilised in HollandPTC, the energy layer switch time is considered to be less than 1 s [24].

Spot Delivery Time
The spot delivery time is the duration during which the proton beam actively delivers radiation to a specific spot. This time is primarily determined by the Monitor Units (MUs) allocated to each spot. The pencil-beam weights are computed by the optimization algorithm and they are equal to the absolute number of protons required in the pencil beam to achieve the desired dose. These weights can be converted to the ionization chamber monitor units under reference conditions [17]. Additionally, the dose rate affects the spot delivery time, which is influenced by the energy layer the spot occupies and the minimum monitor unit for that layer, gmin.

Spot Switching Time
The spot switching time is the time required for the proton beam to move between adjacent spots within an energy layer. This parameter is primarily influenced by the distance between these adjacent spots as well as the speed at which the scanning magnets located inside the nozzle are capable of moving the pencil beam in the x and y direction. Generally, the spot switching time is considered negligible compared to other factors impacting the overall beam delivery time.

Beam Switching Time
The mechanical gantry movement involves rotating the gantry from one angle to another to accurately align the proton beam with the target area. Due to the gantry's large size and complexity, this process naturally takes time. Additionally, the duration is extended because the system must perform safety checks and recalibration after each adjustment.

2.5.2. Robustness
Plan robustness is a crucial element in radiotherapy planning and optimization and should also be taken into account in PAT. Its importance arises from the significant impact of range and patient setup uncertainties on proton therapy. Range uncertainties can arise from various factors, including the conversion of Hounsfield units (HU), a measure of radiodensity in CT scans, to mass stopping power. The mass stopping power is particularly important in proton therapy, and particle therapy in general, because it enables precise predictions of particle range, which are critical for delivering a conformal dose to the target [25]. Additional contributors to range uncertainties include tumor shrinkage and changes in patient weight. Patient setup uncertainties might result from beam and patient anatomy misalignment or intrafractional organ motion. With all these uncertainties possible, the delivered dose distribution might be significantly different from what is seen on the treatment plan which poses a risk on the reliability of proton therapy [26].

Achieving a certain level of OAR robustness is expected to be more challenging for PAT due to the irradiation of the patient from multiple directions compared to IMPT. The increased number of beam angles can introduce more uncertainties in the treatment delivery, including the patient motion, as well as setup errors among others [27].

In conventional photon radiotherapy, setup uncertainties are typically managed by adding margins around the Clinical Target Volume (CTV). These additional margins create what is known as the Planning Target Volume (PTV). The core assumption of

the PTV concept is that the dose distribution shape remains mostly unchanged despite any alterations in the patient's anatomy. Specifically, it is presumed that because the PTV encompasses the CTV, any movement of the CTV within the PTV will still ensure that the CTV receives the prescribed dose, provided the PTV is irradiated as planned [28]. As anticipated, the PTV concept is not suitable for proton therapy. This is because range errors in proton therapy do not merely cause underdosage at the edge of the CTV, which could be mitigated by adding margins. Instead, these range errors can create hot spots (overdose areas) and cold spots (underdose areas) within the target volume.

In proton treatment planning, robust optimization methods are employed to ensure that the plans can effectively withstand a limited range of potential error scenarios [28]. The robustness is assessed by incorporating a setup uncertainty of 0.3 cm with isocenter shifts in 14 different directions on the planning CT scan, 6 in the X, Y, and Z axes and 8 in the diagonal directions as depicted in Figure 2.3. For PBS, a 3% range uncertainty is included to account for CT density shifts. By adding both positive and negative range errors to each setup, a total of 28 scenarios are generated.
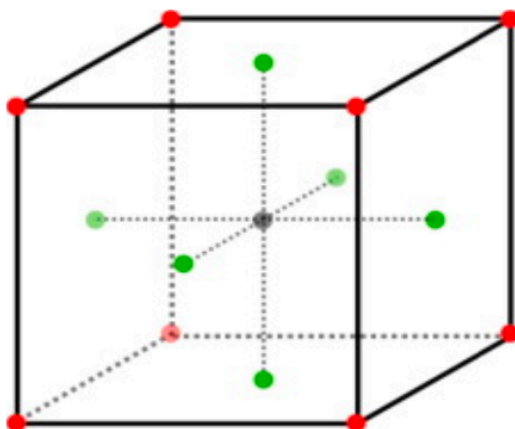
Figure 2.3: Representation of the sampling set up errors in the 6 principal directions (green dots) and in the 8 diagonal directions (red dots) [15]

The robustness of the proton therapy plan is described by the use of the voxelwise metrics. The voxelwise worst-case methods aim to optimize treatment plans to perform as effectively as possible under the most unfavorable physical scenarios. For example, the voxelwise minimum dose represents the lowest dose values per voxel across all scenarios, as illustrated in Figure 2.4 [29]. The approach relies on the worst-case dose distributions, d_{min} and d_{max}, where d_{min} is applied to dose-promoting functions (like minimum dose constraints), and d_{max} is used for dose-limiting functions (such as maximum dose constraints). However, these methods tend to produce overly conservative plans [30].
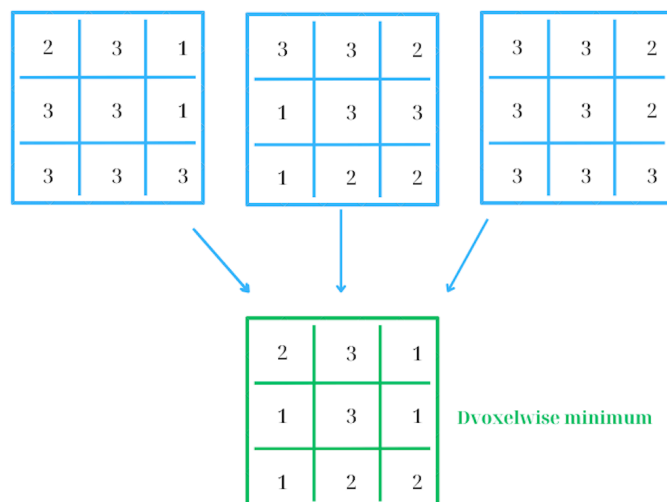
Figure 2.4: Example of the voxelwise minimum dose for three scenarios [29].

2.5.3. LET and RBE

According to ICRU Report No. 85, LET is defined as a nonstochastic quantity representing the average energy transferred through electronic interactions, ionizations or excitations, per unit path length traveled by charged primary particles. This definition applies strictly at a specific spatial point, for a specific material, and for protons of a given energy. However, in practice, finite irradiation volumes, varying tissue types, and protons with a range of energies are considered, making the definition impractical. Hence, LET is commonly averaged over a target volume and two different LET concepts, derived from the original definition of LET, are being applied [31]. Starting with the track-averaged LET, LET_t, it is the LET from each particle weighted with respect to its track length in each voxel. However, the biological effectiveness of a radiation field is primarily influenced by high LET particles, contributing to more complex and lethal chromosomal aberrations. To better connect biological effects with the radiation quality of proton beams, the dose-averaged LET, LET_d, is used. This is calculated by weighting the LET of each particle according to its contribution to the local dose within each voxel [32].

Although high LET regions targeting the tumor volume are considered beneficial, they can pose risks if concentrated near critical structures within high-dose regions. Initial findings suggest that proton therapy could carry an increased risk of radiation-induced toxicities, such as brainstem necrosis in patients treated for brain tumors. This risk may be due to the accumulation of high LET_d values at the brainstem [33]. Delivering proton beams in an arc fashion could potentially reduce the concentration of high LET_d regions, by spreading them out, thereby decreasing toxicity while improving target conformity.

An increased radiosensitivity as a product of high LET_d values, alters the proton dose needed to achieve the same biological effect as photons, which is quantified as the

Relative Biological Effectiveness. The RBE, $\frac{D_{\text{photons}}}{D_{\text{protons}}}\Big|_{\text{isoeffect}}$ [34], is critically important because any inaccuracies in its value could result in a proton dose that is either too low or too high, greatly impacting the effectiveness of proton therapy.

Historically, an RBE value of 1.1 has been adopted by most proton therapy centers, which signifies that protons are considered to be 10% more efficient than photons. Recent experiments and clinical studies [35, 36], have shown that towards the distall fall-off region of the spread-out Bragg peak, the RBE could take values of up to 1.7, leading to toxicities that cannot be easily predicted given the data that is currently used.

Various empirical RBE models have been developed to enhance the accuracy of RBE calculations in human tissue, with one of the most widely used being the McNamara model [37]. The McNamara model is a phenomenological model based on the linear quadratic model, $SF_d = e^{-\alpha d + \beta d^2}$, and a highly comprehensive input database. In this model, a compilation of all RBE experimental measurements available before 2014 was used for a nonlinear regression fit of the RBE as a function of the proton dose D_p, LET_d, and the ratio $\left(\frac{\alpha}{\beta}\right)_x$, with the latter representing the sensitivity of the "x" tissue to radiation. The McNamara model is calculated as:

$$RBE = \frac{1}{2D_p}\left(\sqrt{\left(\frac{\alpha}{\beta}\right)_x^2 + 4D_p\left(\frac{\alpha}{\beta}\right)_x RBE_{\text{max}} + 4D_p^2 RBE_{\text{min}}^2} - \left(\frac{\alpha}{\beta}\right)_x\right) \quad (2.1)$$

where the RBE$_{\text{max}}$ and RBE$_{\text{min}}$ are given as:

$$RBE_{min} = p_2 + p_3\sqrt{\left(\frac{\alpha}{\beta}\right)_x} LET_d \quad (2.2)$$

$$RBE_{max} = p_0 + p_1\frac{LET_d}{\left(\frac{\alpha}{\beta}\right)_x} \quad (2.3)$$

The parameters p_0, p_1, p_2 and p_3 in the Equations 2.2 and 2.3 are well defined by the model. The LET$_d$, is given by

$$LET_d(z) = \frac{\int_0^\infty S_{\text{el}}(E)D(E,z)\,dE}{\int_0^\infty D(E,z)\,dE} \quad (2.4)$$

where $S_{\text{el}}(E)$ is the electronic stopping power of primary protons with kinetic energy E, and D(E,z) is the absorbed dose contributed by primary protons with kinetic energy E at location z [31].

3

Materials and Methods

3.1. Patient Data and Dose Prescription

This study includes data from 10 anonymized neurological cancer patients. The patients were labeled sequentially as P1 to P12, with P3 and P11 excluded as they did not meet the criteria for an AA diagnosis. Conventional IMPT treatment plans were created at HollandPTC and delivered using Varian's ProBeam system. The patients received adjuvant therapy using a single-field, robustly optimized IMPT plan, with a 33x1.8 Gy fractionation scheme, typically following surgical resection. Three distinct beam angles, spaced at least 90 degrees apart to minimize high LET region buildup, were used per patient, tailored to each tumor's location. All clinical plans incorporated a range shifter and included couch rotation adjustments.

3.2. Treatment Plan Preparation

3.2.1. Imaging

For the treatment planning, patients were fixed using custom-made mask fixation, an example of which is shown in Figure 3.1, and underwent pre-treatment CT and MRI.

CT Scanner

At HollandPTC, a Siemens SOMATOM Definition Edge 128-slice dual-energy CT scanner is utilized. This is a single-source TwinBeam system capable of simultaneous acquisition with two energy spectra, however this feature is not employed for this patient category.

MRI scanner

The MRI scanner used in HollandPTC is a Philips-Ingenia MR-RT wide-bore 3T scanner that offers the imaging possibility in treatment position, with the patient being set up based on external lasers.
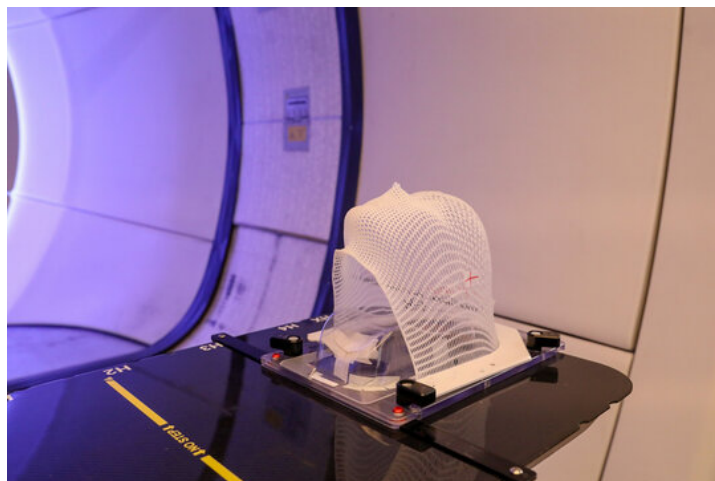
Figure 3.1: Fixation mask used in proton therapy for treating glioma patients. The red cross marks the laser lines that guide the patient's positioning.

3.2.2. Treatment Planning

The treatment plans were generated using the RayStation software (RaySearch Laboratories, Stockholm/Sweden), an advanced commercial treatment planning system that supports proton planning for various proton therapy techniques, including PAT in research mode. Regarding PAT and for a discrete arc beam, RayStation includes parameters such as the start and stop gantry angles, the number of discrete directions as well as the number of energy layers among others. Careful adjustment of these parameters, along with user-defined objectives and constraints, is essential to achieving the optimal treatment plan.

Relevant Parameters

The treatment plans were optimized through a maximum of 120 iterations. During this process, parameters such as beam configurations, beam weights, number of energy layers, and spots were determined. Spot filtering begins after 70 iterations, at which point certain spots and energy layers are removed. The minimum spot meterset, defined as the minimum number of MUs per spot, was set to 3, while the maximum was set to 40. This restriction on the minimum and maximum MUs per spot limits the extent to which the additional degrees of freedom can be utilized in PAT.

Monte Carlo (MC) dose calculations were conducted using a 2 mm dose grid, providing high-resolution results but requiring great computational power and long calculation times. The computational time for the MC algorithm scales roughly with the inverse cube of the dose grid size [38].

For the plans generated in this project, a single beam with multiple discrete directions was created. The gantry was initially positioned at a 180-degree angle and is capable of rotating fully in either a clockwise or counterclockwise direction, with the latter option being applied in this project. The optimization process identified the best angle configuration based on the chosen number of discrete directions. These discrete beam angles were independent of the tumor location, determined solely by the number of selected beam directions. The beam angles were calculated by dividing the full

360-degree rotation by the total number of directions chosen.

For each number of discrete directions, a suitable initial and final number of energy layers was selected, with the initial count set to be double that of the final count, following RayStation's specifications. Therefore, the planning system starts with a higher number of energy layers and after the 70 iterations it ends up with the optimal number of energy layers and spots. The process used to determine the optimal number of final energy layers based on the number of discrete beam directions followed a trial-and-error approach. Specifically, a certain number of final layers was selected for each beam setup, with RayStation providing the guideline that 11 beam directions should correspond to a final number of 360 energy layers. If the number of energy layers achieved after 120 iterations was significantly lower than the chosen value, the number of layers was reduced. Conversely, if the total number of energy layers achieved matched the set target, the number of layers was increased.

For each patient, six distinct treatment plans were created, each with a different number of beam directions and an appropriate final number of energy layers. These plans included 6, 9, 18, and 27 beam directions. Additionally, two more plans were created: one with 9 beam directions and a 3 cm range shifter, and another with 18 directions and the same range shifter thickness. The purpose of these two additional plans was to assess whether a range shifter is beneficial for the PAT of glioma patients.

The clinical plan used for treating the patients was already available in the software, with a minor adjustment in the dose grid used for the dose calculation. To ensure a fair comparison between the PAT plans and the clinical plan, the dose for the clinical plan was recalculated using a 2 mm dose grid instead of the original 1 mm grid.

Organ Contouring
The software enables contouring of the OARs and other relevant structures. Radiation oncologists had already contoured the organs on each patient's pre-treatment CT scan, which was then aligned with the pre-treatment MRI scan, for a better visualization of the soft tissues. All the PAT plans generated for this project were based on these existing contours.

Clinical Goals
The list of clinical goals for the neuro-oncological patients was already present in the software and is shown in Table 3.1.

Table 3.1: Clinical goals for patients with neurological tumors.

Priority	Region of Interest	Clinical goal
1	CTV coverage	At least 98.00% volume at 56.43 Gy (RBE) dose
1	CTV max dose	At most 63.56 Gy (RBE) dose at 2.00% volume
2	Brainstem Core	At most 54.00 Gy (RBE) dose at 0.03 cm^3 volume
2	Brainstem Surface	At most 60.00 Gy (RBE) dose at 0.03 cm^3 volume
2	Left Lens	At most 10.00 Gy (RBE) dose at 0.03 cm^3 volume
2	Right Lens	At most 10.00 Gy (RBE) dose at 0.03 cm^3 volume
2	Optic Chiasma	At most 55.00 Gy (RBE) dose at 0.03 cm^3 volume
2	Left Optic Nerve	At most 55.00 Gy (RBE) dose at 0.03 cm^3 volume
2	Right Optic Nerve	At most 55.00 Gy (RBE) dose at 0.03 cm^3 volume
2	Left Retina	At most 45.00 Gy (RBE) dose at 0.03 cm^3 volume
2	Right Retina	At most 45.00 Gy (RBE) dose at 0.03 cm^3 volume
2	Spinal Cord Core	At most 54.00 Gy (RBE) dose at 0.03 cm^3 volume
2	Spinal Cord Surface	At most 60.00 Gy (RBE) dose at 0.03 cm^3 volume
3	Brain - CTV	At most 0.00 Gy (RBE) average dose
3	Cerebrum - CTV	At most 0.00 Gy (RBE) average dose
3	Left Cochlea	At most 45.00 Gy (RBE) average dose
3	Right Cochlea	At most 45.00 Gy (RBE) average dose
3	Left Cornea	At most 30.00 Gy (RBE) dose at 0.03 cm^3 volume
3	Right Cornea	At most 30.00 Gy (RBE) dose at 0.03 cm^3 volume
3	Left Gland Lacrimal	At most 30.00 Gy (RBE) average dose
3	Right Gland Lacrimal	At most 30.00 Gy (RBE) average dose
3	Hippocampi	At most 7.40 Gy (RBE) dose at 40.00% volume
3	Hippocampi - CTV	At most 0.00 Gy (RBE) average dose
3	Left Hippocampus	At most 7.40 Gy (RBE) dose at 40.00% volume
3	Right Hippocampus	At most 7.40 Gy (RBE) dose at 40.00% volume
3	Pituitary	At most 20 Gy (RBE) average dose
3	Skin	At most 50.00 Gy (RBE) dose at 0.03 cm^3 volume

The clinical goals were organized into three priority levels, with priority ones acting as constraints: $V_{95\%} \geq 98\%$ and $D_{2\%} \leq 107\%$ of the prescribed dose, where $V_{95\%}$ is the volume that receives at least 95% of the prescribed dose and $D_{2\%}$ is the dose received at 2% of the target volume.

Priority level two refers to the serial OARs, specifically the brainstem core and surface, the left and right lenses, the optic chiasm, the left and right optic nerves, the left and right retinas, and the spinal cord core and surface. For this priority, a maximum dose limit was set at a volume of 0.03 cm^3.

The third category includes the remaining OARs, with particular emphasis on the dose received by the healthy brain, hippocampi, pituitary gland, and skin.

3.2.3. Delivery Time Calculation

The delivery duration was determined using a script developed by MSc student, Gianna Eeken, which is included in Appendix A. The selected time parameters included an ELST of 0.78 seconds [15], a beam switching time of 45 seconds, specified by Varian, and a spot switching time based on a scanning magnet speed of 500 cm/s in the x direction and 2000 cm/s in the y direction [39], as well as data on the distances between adjacent spots. Two different methods were used to determine the spot delivery time. The first measurement relied on the dose rate in MU/min per energy layer for the Varian ProBeam system, as illustrated in Figure 3.2. The second focused on regions within the same figure where the dose rate reached saturation. As depicted in Figure 3.2, the proton dose rate exhibits a linear relationship with the minimum monitor unit per spot, g_{min}. For the saturated regions, in-house measurements were conducted at higher dose rates, employing an increased global MU threshold.
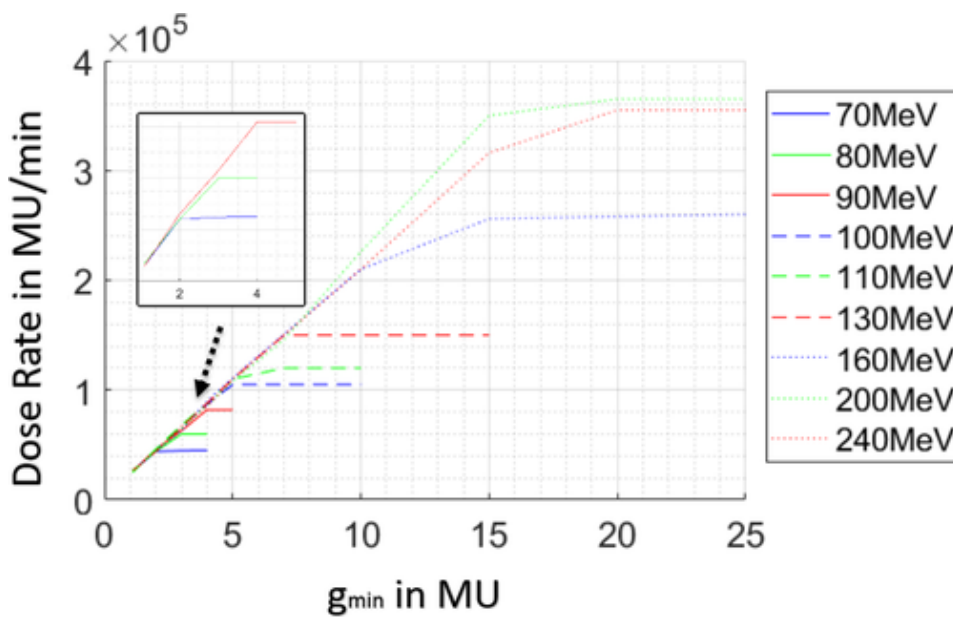
Figure 3.2: The linear dependence of pencil beam scanning dose rate on MU threshold gmin for Varian ProBeam system. The black box contains zoomed-in view of 70-90 MeV [40].

To verify that the delivery times calculated by the script matched the actual delivery times, measurements were conducted. Specifically, the plan with the 18-directions for patient 1 was tested to compare the real measurements with the script's outputs. This plan was chosen because the high number of beam directions and energy layers made it more likely to reveal any significant variation. However, no such difference was observed, as the delivery times were found to be consistent.

Couch Rotation Time
For clinical plans, all of which included couch rotations, an extra time factor was considered. The time needed for these rotations was determined by the fact that rotating the couch 90 degrees requires 60 seconds.

3.2.4. Robustness

The robustness analysis considered three key CTV metrics: the $V_{95\%}$, $D_{2\%}$, and $D_{98\%}$ which were assessed in both the nominal scenario and the voxelwise minimum/maximum. The $V_{95\%}$ ensures sufficient CTV coverage by confirming that a minimum volume of the target receives an adequate percentage of the prescribed dose. Meanwhile, the $D_{2\%}$ is significant because it highlights "hot spots", or areas within the CTV that are overdosed. These two metrics were included in the clinical goals, with the $D_{98\%}$ easily added manually. More specifically, the $D_{98\%}$ which corresponds to the dose received by 98% of the target volume was set to be higher than 95% of the prescribed dose, which equals 56.43 Gy. The significance of selecting the $D_{98\%}$ as a metric lies in its ability to ensure that 98% of the target volume receives a sufficient dose, while indicating "cold-spots" in the CTV. The clinical goals specified the values of these three metrics in the nominal scenario. The software allows dose calculations across the 28 evaluation scenarios, along with the voxelwise minimum and maximum. For the $V_{95\%}$ and $D_{98\%}$, the voxelwise minimum was applied since these metrics are dose-promoting whereas for the $D_{2\%}$, the voxelwise maximum was used due to its dose-limiting purpose.

3.2.5. LET Analysis

The LET analysis started by generating isodose volumes using a software tool that enabled the creation of thresholds based on specific percentages of the prescribed dose, namely the 60% and 90%. For each treatment plan, the intersections of these isodose volumes with the healthy brain tissue resulted in two overlapping volumes. The LET_d values from specific volumes within these overlaps, namely 0.03, 0.1, 1, and 10 cc, were then extracted. These values were obtained using LET Volume Histograms (LVHs) and exported into Excel files, which included the LET_d values and their corresponding absolute volumes. An example of a representative LVH is given in the figure below.
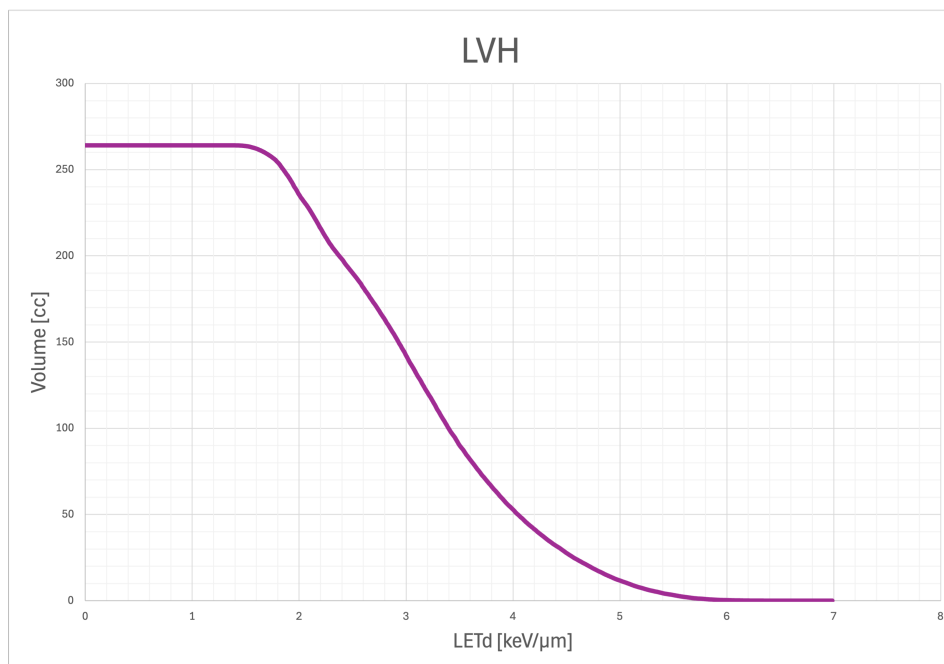
Figure 3.3: An example of an LVH

The selection of these isodose volumes was made to accurately represent the high-dose regions of the brain, ensuring that the LET values were obtained only from these areas. This is because high LET values are only meaningful within high-dose regions.

An additional analysis of the isodose volumes was conducted to verify whether the findings of [21], which suggest a decrease in the isodose volumes with an increase in the number of beam directions, are applicable to this project. The results are shown in Appendix E.

3.3. Statistical Analysis

A statistical analysis was incorporated into the project to support the comparisons. This analysis was conducted for the 280 in total evaluation scenarios (10 patients x 28 scenarios each) of the $V_{95\%}$, $D_{2\%}$, and $D_{98\%}$ metrics, as the available data was sufficient for this purpose. However, no statistical analysis was performed in the rest of the project since the amount of data was not sufficient.

The steps followed for the statistical analysis are explained in the hierarchical graph below, Figure 3.4.
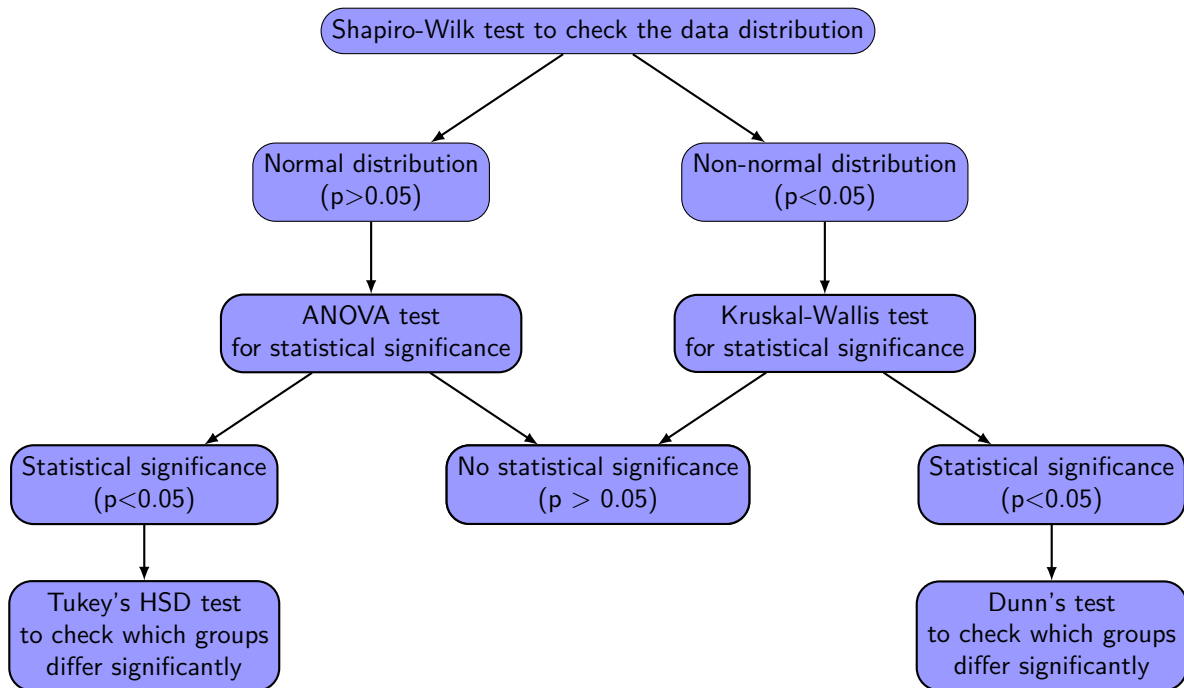
Figure 3.4: The statistical analysis steps that were followed in this project.

An additional metric utilized in the statistical analysis to represent data dispersion is the InterQuartile Range (IQR). The IQR is calculated as the difference between the 75th and 25th percentiles, representing the range containing the central 50% of the data. Thus, a larger IQR indicates greater variability within the data.

4

Results

4.1. Duration of the Plans and their Time Components

Table 4.1 presents the median, minimum, and maximum delivery times, in minutes, for the clinical and the PAT plans, along with the IQR.

In the following tables showing the delivery times and time differences, the values represent fractions of a minute. For example, a median clinical delivery time of 5.13 minutes means 5 minutes and 0.13 minute, which is approximately 8 seconds.

Table 4.1: Median, minimum and maximum delivery times [min] per plan for the total of 10 patients. The table also includes the IQR as a measure of data dispersion.

Plan	Median	Minimum	Maximum	IQR
Clinical	5.13	4.26	5.66	0.49
6 directions	7.56	6.75	7.89	0.21
9 directions	11.16	10.06	11.57	0.36
18 directions	21.46	19.25	22.25	0.51
27 directions	30.29	28.98	30.36	0.15
9 directions, range shifter	10.91	9.94	11.38	0.24
18 directions, range shifter	20.97	19.47	21.43	0.69

The boxplots of Figure 4.1 offer a graphical representation of Table 4.1.
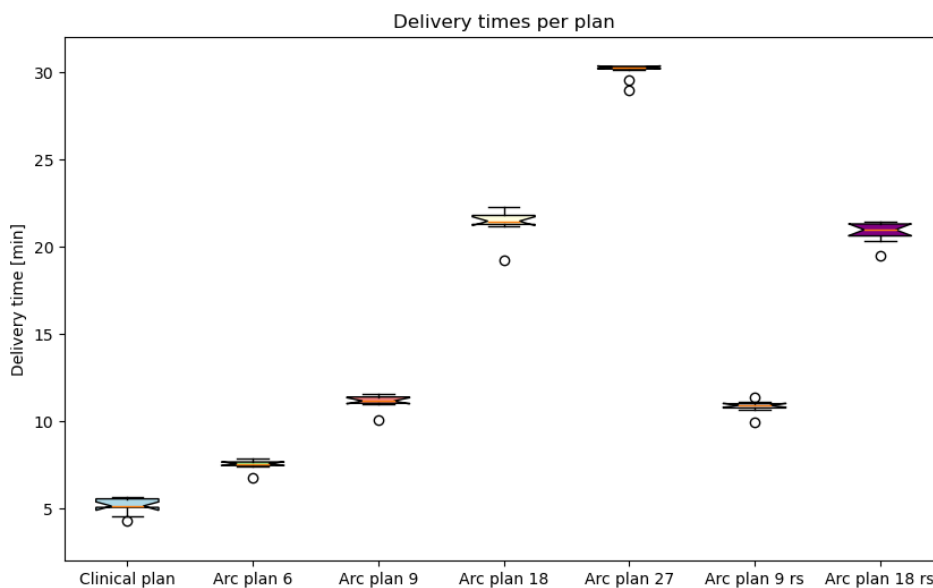
Figure 4.1: Boxplots of the delivery times [min] per plan, for the total of 10 patients.

The delivery times displayed in both Table 4.1 and Figure 4.1 represent a combination of the previously discussed time parameters. The contribution of each parameter to the total tdelivery duration is given in Figure 4.2. The figure refers to patient 1, though similar patterns are also observed in the rest of the patient population, as can be seen in Appendix B.
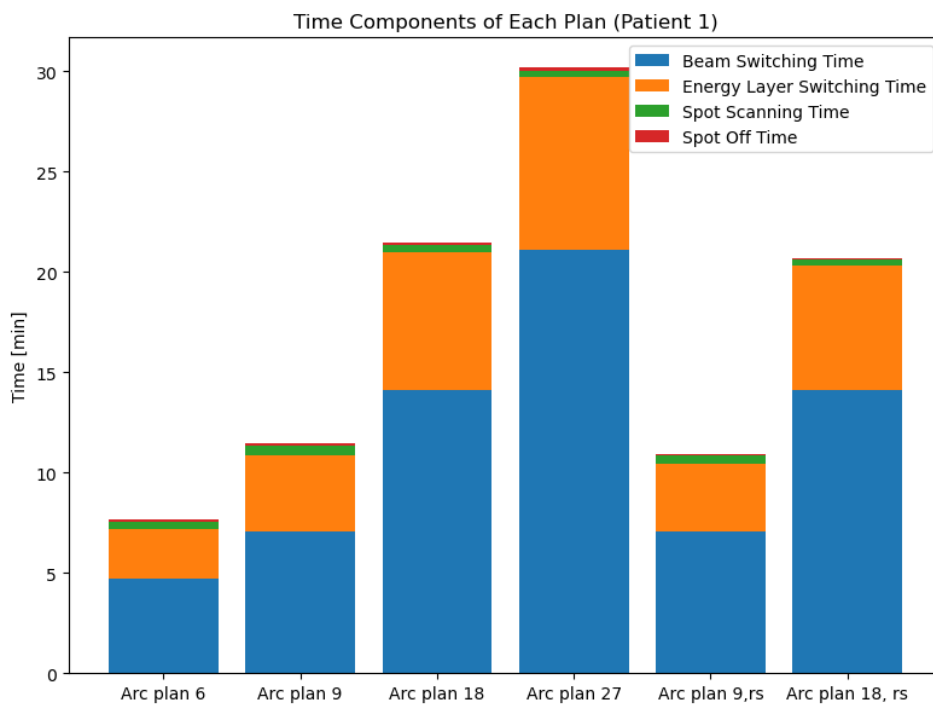
Figure 4.2: Delivery time components [min] per PAT plan, for patient 1.

As the beam switching time constitutes the majority of the delivery duration, the time

saved by reducing the beam switching time from 45 seconds to 20 seconds was calculated for each plan.

Table 4.2: Delivery time difference (in minutes) between beam switching times of 45 s and 20 s.

Plan	Time Difference (min)
Clinical	0.83
6 directions	2.08
9 directions	3.33
18 directions	7.08
27 directions	10.83
9 directions, range shifter	3.33
18 directions, range shifter	7.08

In determining the contribution of the beam switching time to the total delivery duration, only the number of beams is significant. Thus, across the entire patient population, all plans with the same arc configuration exhibit an identical time difference.

With the energy layer switching time being the second most significant component in the delivery duration, a similar analysis was conducted to determine the median, minimum, and maximum time differences, in minutes, across all patients between plans with an ELST of 0.78 s and those with 0.6 s. The results are summarized in Table 4.3.

Table 4.3: Median, minimum and maximum delivery time difference [min] using an ELST of 0.78 s and 0.6 s.

Plan	Median	Minimum	Maximum	IQR
Clinical	0.28	0.24	0.32	0.03
6 directions	0.55	0.4	0.61	0.05
9 directions	0.85	0.62	0.94	0.09
18 directions	1.58	1.12	1.74	0.11
27 directions	2.01	1.75	2.02	0.03
9 directions, range shifter	0.77	0.59	0.86	0.06
18 directions, range shifter	1.48	1.16	1.55	0.16

4.2. Robustness

4.2.1. Voxelwise Robustness Analysis of the $V_{95\%}$, $D_{2\%}$, and $D_{98\%}$

Figures 4.3 and 4.4 present boxplots of the $V_{95\%}$ values for the entire patient cohort, categorized by plan. Each plan is distinguished by a different color, as described in the legend. The legend also explains the black dashed line, which represents the clinical goal of the $V_{95\%}$. Figure 4.3 shows results for the nominal scenario, whereas Figure 4.4 depicts the voxelwise minimum.
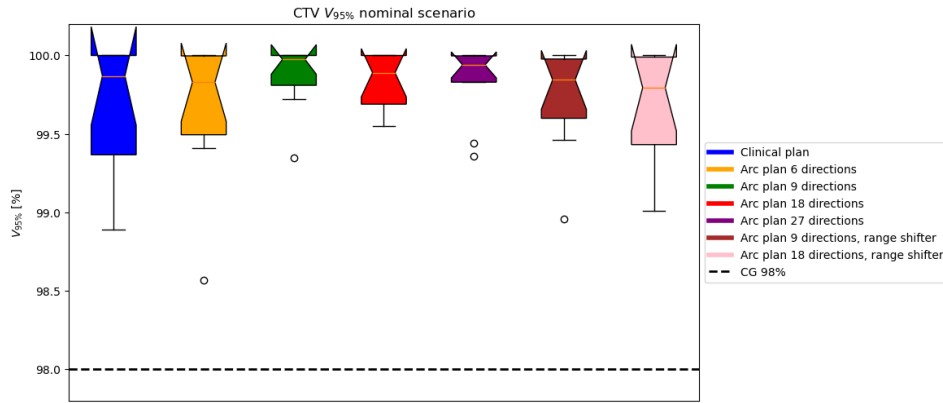
Figure 4.3: Boxplots of the $V_{95\%}$ [%] nominal values per plan, across the patient population.
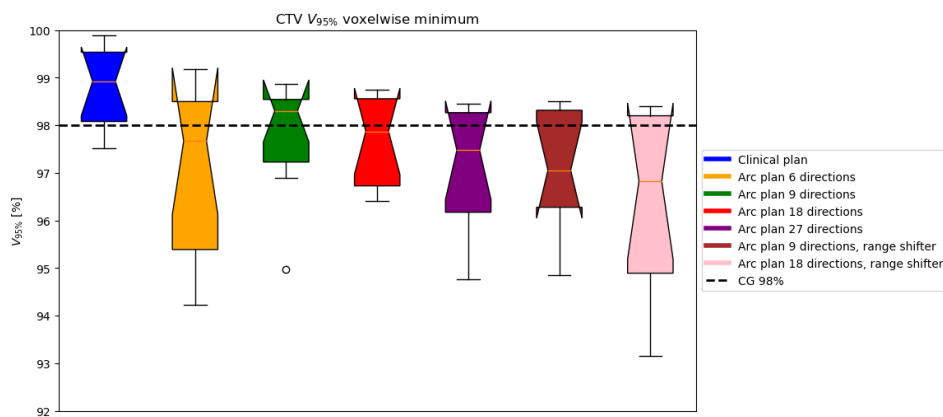
Figure 4.4: Boxplots of the $V_{95\%}$ [%] voxelwise minimum values per plan, across the patient population.

Another representation of Figures 4.3 and 4.4 is given in Tables C.1 and C.2 in Appendix C.

The same analysis followed for the $V_{95\%}$ was also followed for the $D_{2\%}$ and $D_{98\%}$. The figures below illustrate this, with Figures 4.5 and 4.7 referring to the nominal scenarios and Figures 4.6 and 4.8 to the voxelwise maximum and minimum of the $D_{2\%}$ and $D_{98\%}$ respectively.
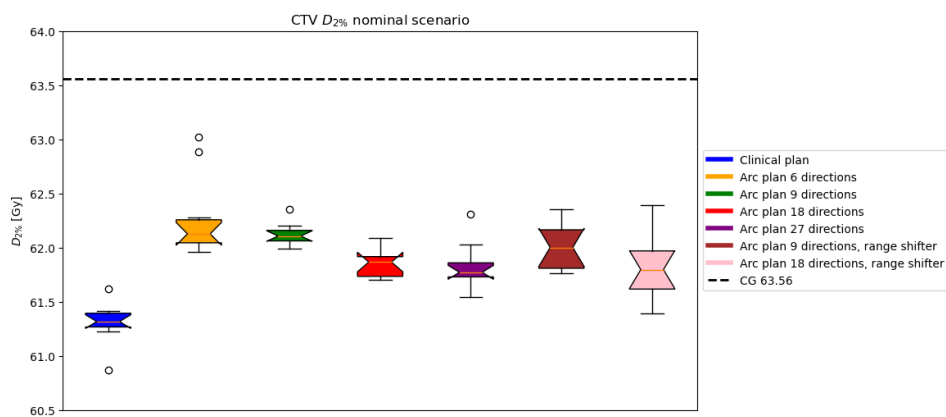
Figure 4.5: Boxplots of the $D_{2\%}$ [Gy] nominal values per plan, across the patient population.
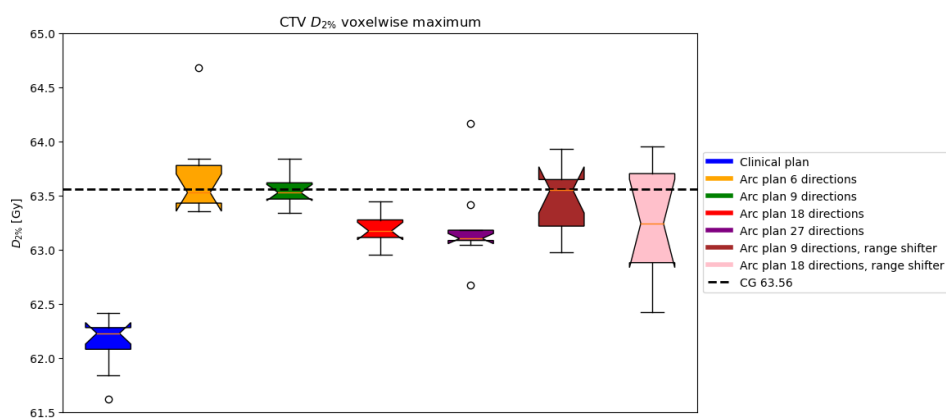
Figure 4.6: Boxplots of the $D_{2\%}$ [Gy] voxelwise maximum values per plan, across the patient population.

The clinical goal for the $D_{2\%}$ was set to 63.56 Gy which corresponds to 107% of the prescribed dose.
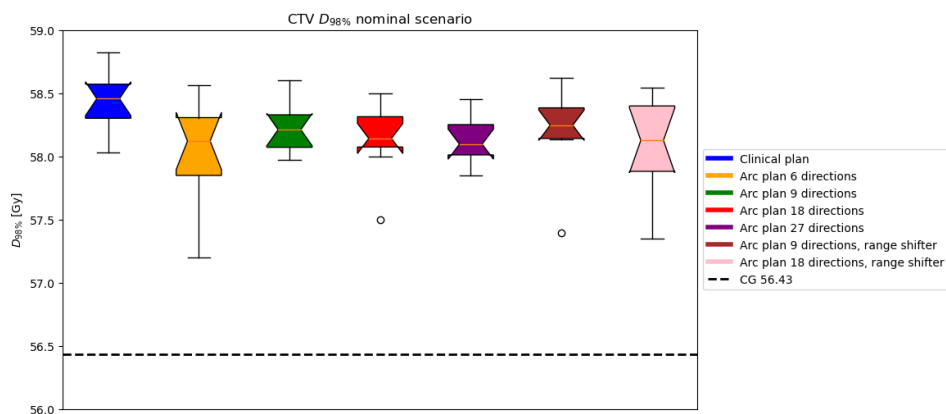
Figure 4.7: Boxplots of the $D_{98\%}$ [Gy] nominal values per plan, across the patient population.
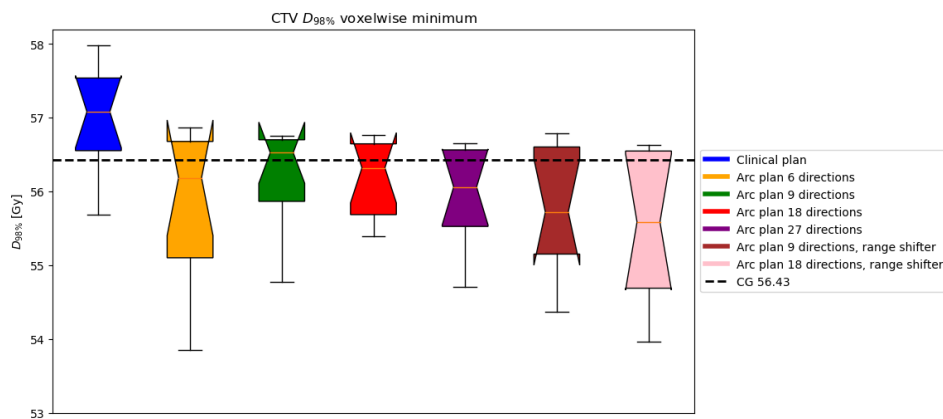
Figure 4.8: Boxplots of the $D_{98\%}$ [Gy] voxelwise minimum values per plan, across the patient population.

The clinical goal for the $D_{98\%}$ was set to 56.43 Gy which corresponds to 95% of the prescribed dose.

4.2.2. Scenario-based Robustness Analysis of the $V_{95\%}$, $D_{2\%}$, and $D_{98\%}$

An additional analysis was performed based on the 28 evaluation scenarios of each plan for every patient. The $V_{95\%}$, $D_{2\%}$, and $D_{98\%}$ metrics were examined, as illustrated in the figures below.
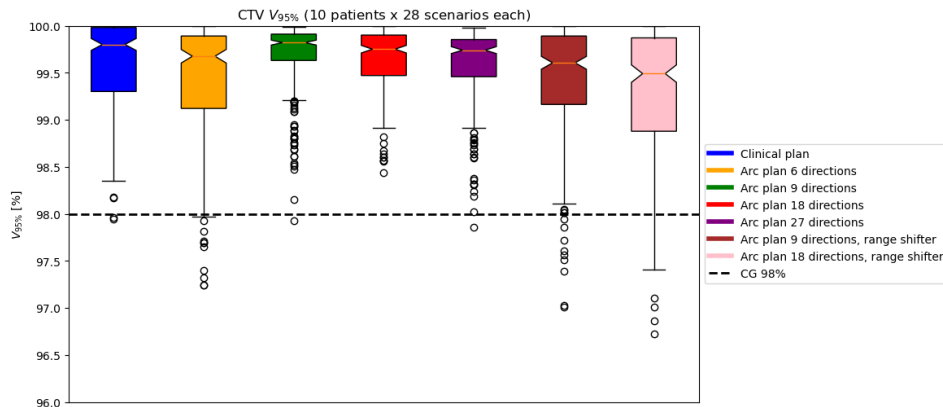
Figure 4.9: Boxplots of the $V_{95\%}$ [%] based on the 28 evaluation scenarios of each patient across the whole population.

Given the sufficient volume of data for statistical analysis, Shapiro-Wilk tests were conducted to evaluate the data distribution. The results revealed that none of the plans across the 280 evaluation scenarios for the $V_{95\%}$ followed a normal distribution. According to the statistical analysis summarized in Figure 3.4, a Kruskal-Wallis test was subsequently performed, revealing significant differences between the groups. Dunn's post-hoc test further identified that the clinical plan significantly differs from the 6-directions plan, the 27-directions plan, and the plans including range shifters.
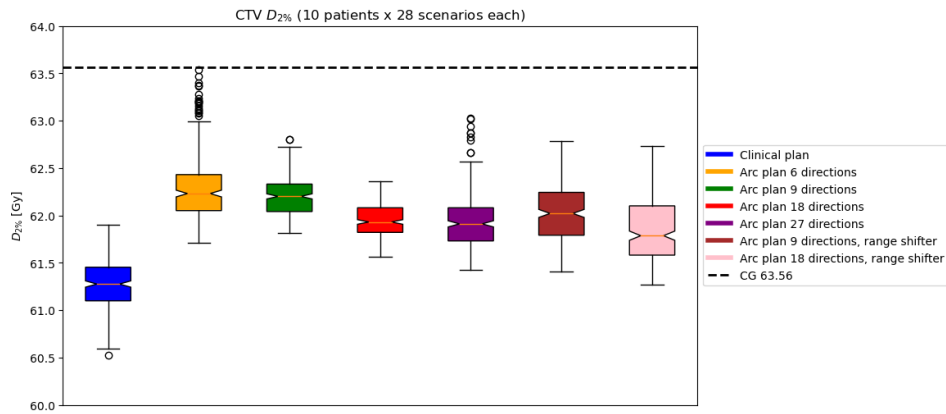
Figure 4.10: Boxplots of the $D_{2\%}$ [Gy] based on the 28 evaluation scenarios of each patient across the whole population.
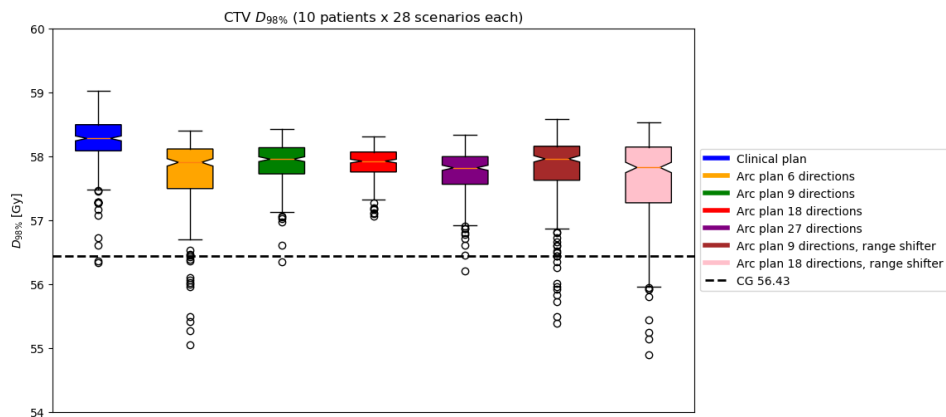
Figure 4.11: Boxplots of the $D_{98\%}$ [Gy] based on the 28 evaluation scenarios of each patient across the whole population.

The Shapiro-Wilk test results for the $D_{2\%}$ and $D_{98\%}$ revealed that all plans exhibited a non-normal distribution. As a result, the Kruskal-Wallis tests were conducted, showing statistically significant differences, which were further explored using Dunn's post-hoc tests. The clinical plan was found to differ significantly from all other plans in both cases.

4.3. LET and RBE distributions

4.3.1. LET

The figures below present the LET_d values for the intersection of the 60% prescribed dose isodose volume, unique to each plan, with the healthy brain volume. These values are shown for specific absolute volumes of the overlap structures. An alternative representation of these boxplots is available in Appendix D.
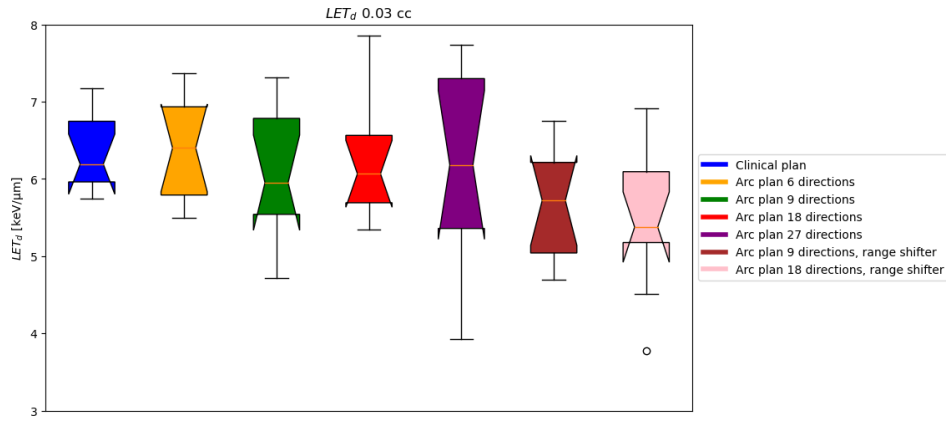
Figure 4.12: Boxplots of the LET$_d$ values for a 0.03 cc volume at the intersection of the 60% isodose volume with the healthy brain volume.
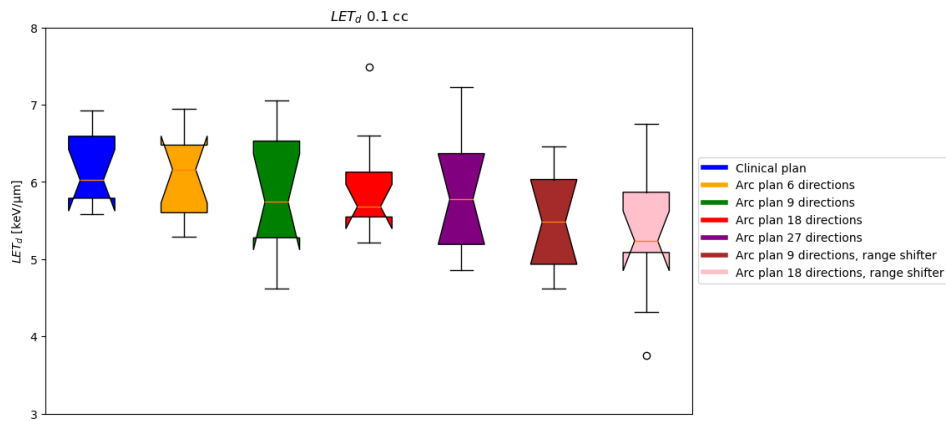
Figure 4.13: Boxplots of the LET$_d$ values for a 0.1 cc volume at the intersection of the 60% isodose volume with the healthy brain volume.
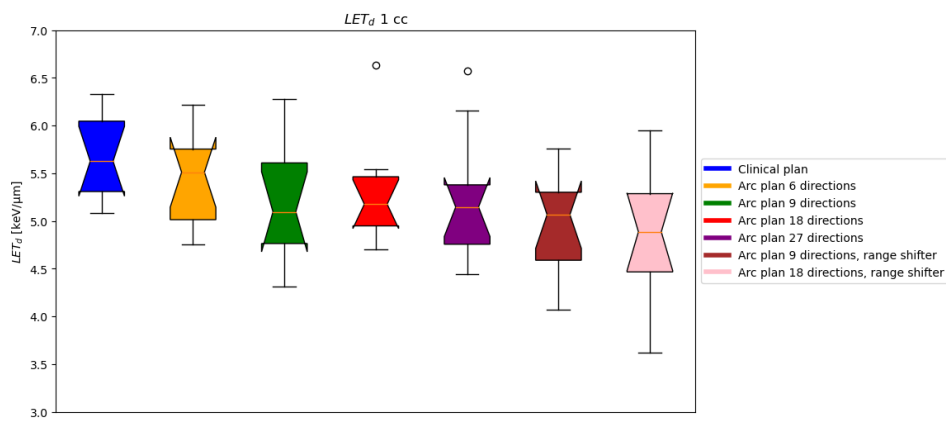
Figure 4.14: Boxplots of the LET$_d$ values for a 1 cc volume at the intersection of the 60% isodose volume with the healthy brain volume.
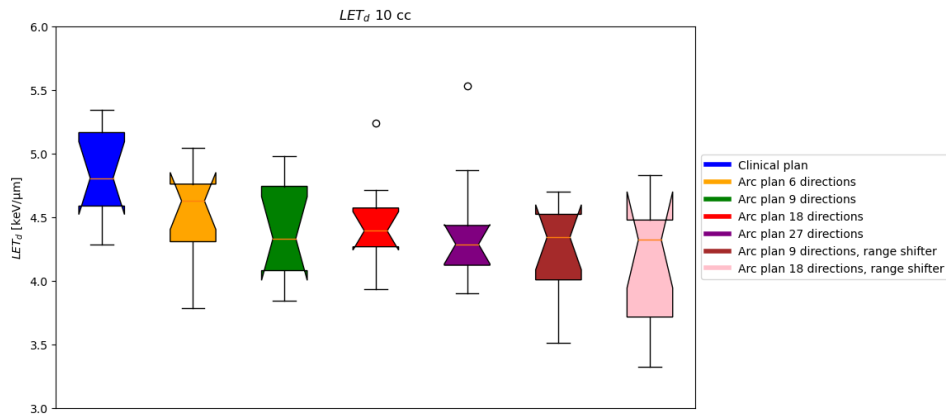
Figure 4.15: Boxplots of the LET$_d$ values for a 10 cc volume at the intersection of the 60% isodose volume with the healthy brain volume.

The same analysis was also followed for the intersection of the 90% prescribed dose isodose volume with the healthy brain volume. The LET$_d$ values for the same absolute volumes of the overlap structures are shown in the figures below and in Appendix D.
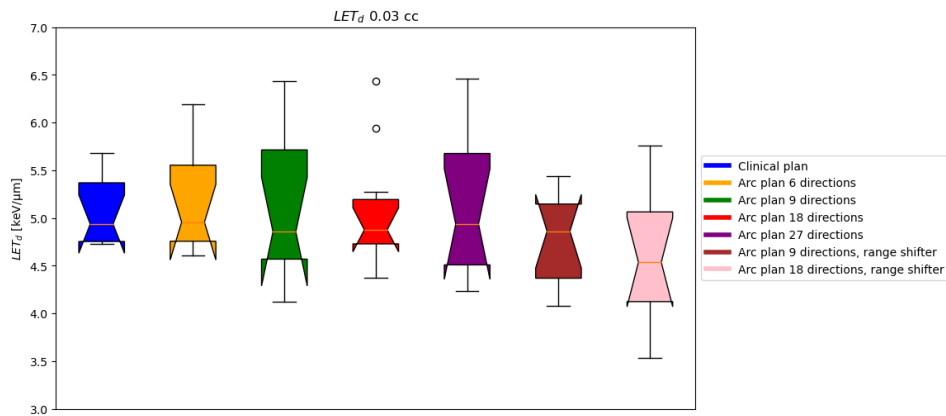
Figure 4.16: Boxplots of the LET$_d$ values for a 0.03 cc volume at the intersection of the 90% isodose volume with the healthy brain volume.
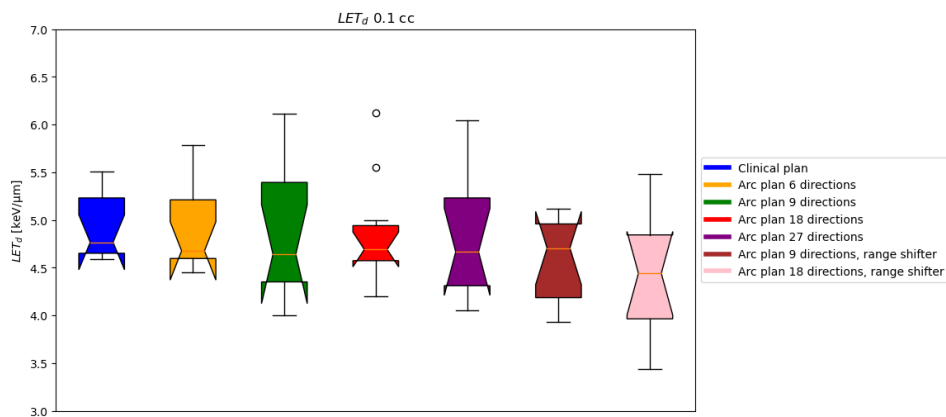
Figure 4.17: Boxplots of the LET$_d$ values for a 0.1 cc volume at the intersection of the 90% isodose volume with the healthy brain volume.
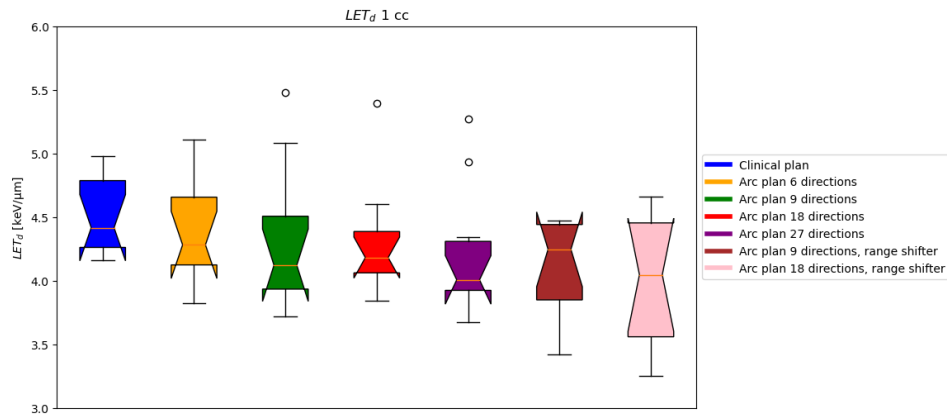
Figure 4.18: Boxplots of the LET$_d$ values for a 1 cc volume at the intersection of the 90% isodose volume with the healthy brain volume.
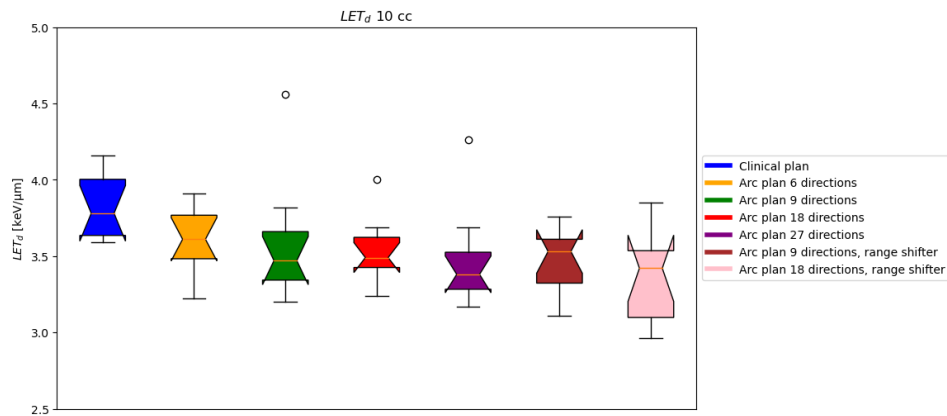
Figure 4.19: Boxplots of the LET$_d$ values for a 10 cc volume at the intersection of the 90% isodose volume with the healthy brain volume.

4.3.2. Effective RBE

The figures below display the fraction of the McNamara dose with the RBE 1.1 dose, both calculated at 0.03 cc volumes for the five OARs of interest: the brainstem core and surface, the optic chiasma, and the two optic nerves. The RBE 1.1 dose is calculated by multiplying the physical dose by an RBE factor of 1.1. Therefore the fraction of the two doses is indicative of the effective RBE.

It is important to note that the volumes used for calculating the two doses may differ between the two distributions. This difference could, for instance, be attributed to the presence of MC noise. Such variability represents a limitation of the analysis, though it is driven by clinical considerations.
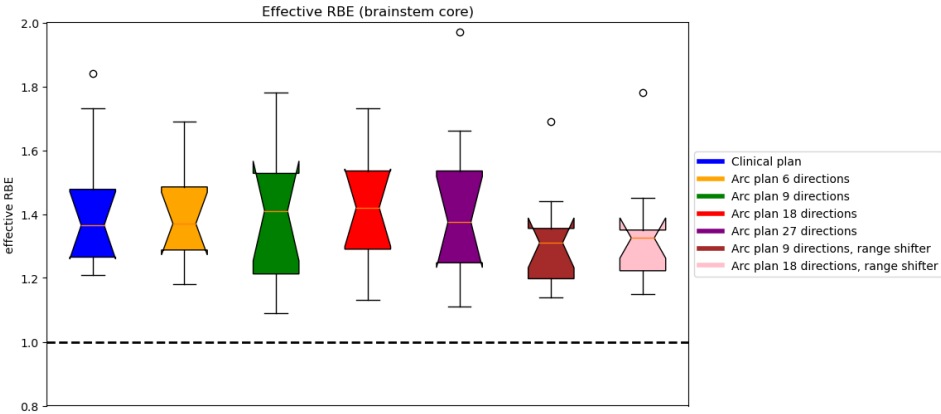
Figure 4.20: Effective RBE per plan across the whole patient population, for the brainstem core.
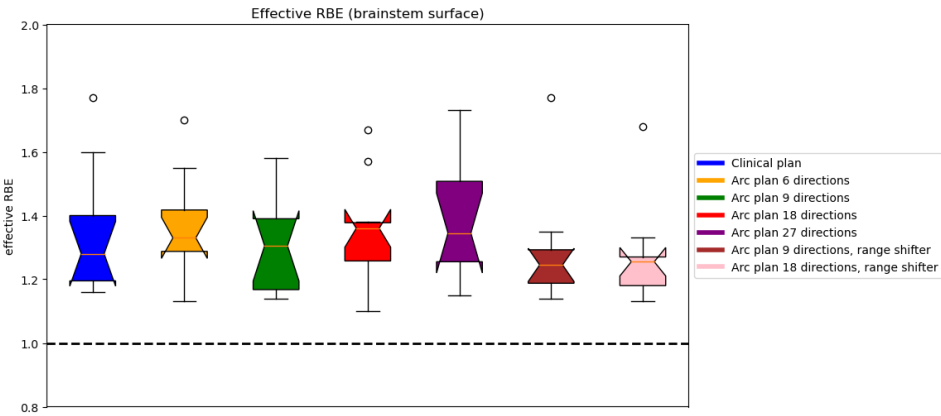
Figure 4.21: Effective RBE per plan across the whole patient population, for the brainstem surface.
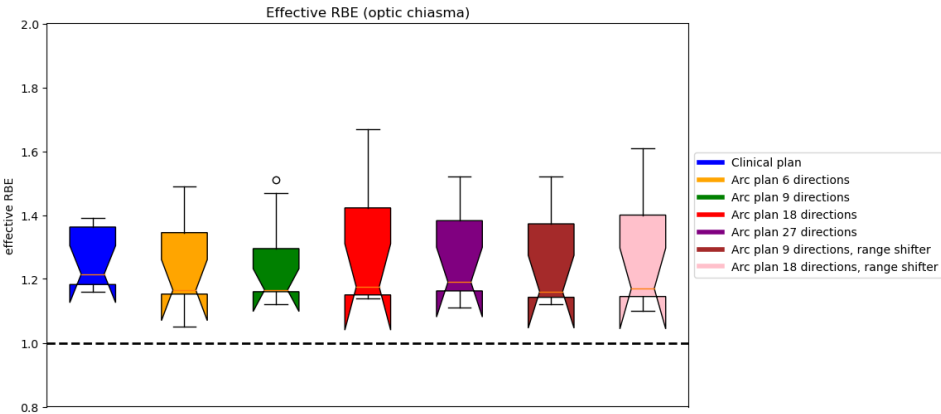
Figure 4.22: Effective RBE per plan across the whole patient population, for the optic chiasma.
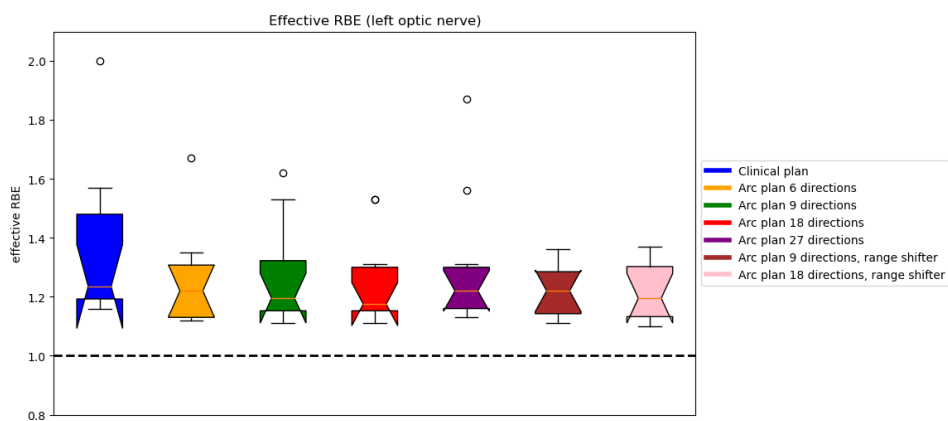
Figure 4.23: Effective RBE per plan across the whole patient population, for the left optic nerve.
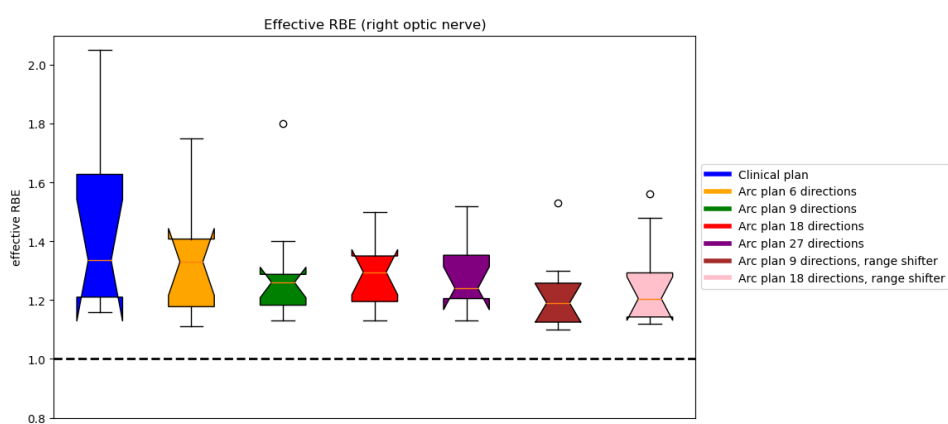
Figure 4.24: Effective RBE per plan across the whole patient population, for the right optic nerve.

Discussion

This section evaluates the treatment times, robustness, and LET/RBE distributions of the PAT plans, with the primary aim of comparing them to the clinical plan. The analysis reveals that the PAT plans generally require longer delivery times due to the increased number of beam directions and longer beam switching times, with the 27-directions plan leading to the longest delivery duration. In terms of robustness, the PAT plans perform well in the nominal scenarios but show more variability when assessed using voxelwise metrics. The LET analysis favors the PAT plans, as they typically result in lower median LET_d values compared to the clinical plan, with particularly positive outcomes for the plans incorporating a range shifter.

5.1. Delivery Times

As anticipated, PAT plans result in longer delivery times. This is clearly demonstrated in both Table 4.1 and Figure 4.1, where it is evident that the clinical plan results in the shortest delivery duration. The PAT plans naturally take longer due to the increased beam directions and significant beam switching times. The longest treatment time is associated with the 27-directions plan, which exceeds 30 minutes. At the start of this project, a target time of 35-40 minutes per plan was considered possibly acceptable, beyond which delivering the treatment could become challenging due to patient setup and comfort concerns.

An additional factor affecting the delivery time of the clinical plan is the inclusion of couch rotation, which is regarded as beneficial for enhancing tumor coverage and reducing exposure to healthy tissue. However, for simplicity, couch rotation was not incorporated into the PAT plans of this project. Future studies that will incorporate it are anticipated to report longer delivery times for PAT plans, potentially at the expense of improved dosimetric quality.

In calculating the delivery times for each plan, the beam switching time is the most significant factor, as each beam angle change introduces roughly 45 seconds of additional waiting. The next most significant factor is the ELST, followed by the time required for spot scanning, while the spot-off time is minimal and can be considered negligible. Therefore, reducing the beam switching time from 45 seconds to 20 sec-

onds could save at least 10 minutes for the 27-directions plan, as shown in Table 4.2. However, reducing the ELST does not result in substantial time savings; a decrease of 0.18 seconds would only save 2 minutes for the 27-directions plan, with even more negligible impact on the other plans.

5.2. Robustness

5.2.1. Nominal Scenario and Voxelwise Metrics

Overall, the robustness evaluation based on the nominal scenario and voxelwise metrics revealed some noteworthy aspects. In all three metrics, the PAT plans meet the clinical goal in the nominal scenario but perform less effectively in the voxelwise assessment. A further interesting finding emerges from the analysis of the $V_{95\%}$. In the nominal scenario, the PAT plans with 9-, 18-, and 27-directions show a higher median value and a smaller variation compared to the clinical plan. However, this trend reverses in the voxelwise minimum evaluation, where all PAT plans result in poorer CTV coverage and a generally larger spread of data.

For the other two metrics, the clinical plan outperforms the PAT plans in both the nominal scenario and the voxelwise evaluation. In case of the $D_{2\%}$, the clinical plan delivers a lower median dose, followed by the 27-directions plan, which performs the best among the PAT plans.

The superiority of the clinical plan is also evident in the robustness evaluation of the $D_{98\%}$, where it shows a higher median value in both the nominal scenario and the voxelwise minimum. Among the PAT plans, the 9-directions plan performs well in the nominal scenario, achieving a high median $D_{98\%}$ and the best result in the voxelwise minimum.

5.2.2. Evaluation of the Voxelwise Minimum/Maximum as Robustness Metrics for the PAT Plans

The behavior of the plans for the $V_{95\%}$ between the nominal scenario and the voxelwise minimum values is somewhat unusual. Although some of the PAT plans perform better than the clinical plan in the nominal scenario, their performance decreases when evaluated using the voxelwise minimum values. This trend is also observed in the other two metrics, where the PAT plans meet the clinical goals in the nominal scenario, but their performance appears to change significantly when assessed with the voxelwise minimum/maximum values.

To further investigate this behavior, the 10th percentile values of the $V_{95\%}$, $D_{2\%}$, and $D_{98\%}$ from the 28 evaluation scenarios across the entire patient cohort, with the voxelwise minimum or maximum were compared. A line was fitted per plan to represent the total of 10 points, one for each patient, which refer to a specific 10th percentile as a function of its voxelwise minimum or maximum. Additionally, a dashed unity line is included in the figures, indicating where the 10th percentile equals the voxelwise minimum or maximum. If the 10th percentile closely aligns with the voxelwise metric this would mean that the voxelwise metric is a reliable reflection of the dose distribution. Therefore, the smaller the angular difference of the plans with this unity line, the more

reasonable the use of the voxelwise metrics in the evaluation of a plan's robustness. The results are shown in Figures C.1, C.2, and C.3 in Appendix C, along with examples of the linear fitting of the 10th percentile points with the voxelwise minimum or maximum.

For the $V_{95\%}$ and $D_{2\%}$, the clinical plan aligned most closely with the unity line, suggesting that the voxelwise minimum and maximum are reliable for representing the robustness of the clinical plan for the $V_{95\%}$ and $D_{2\%}$, respectively. In contrast, these metrics may not be as relevant for the PAT plans. The results for the $D_{98\%}$ were more inconsistent, as the clinical plan did not show the smallest angular difference, and thus no similar conclusion could be drawn.

While this approach may seem like an intuitive method for assessing the reliability of the voxelwise metrics in the robustness evaluation of PAT plans, it lacks precision because it assumes a linear relationship between the 10th percentiles and their corresponding voxelwise metrics. While this assumption may hold true in some cases, in others it is too imprecise to be valid as shown in the figures of Appendix C.

In summary, the voxelwise minimum and maximum metrics appear conservative when applied to PAT plans, potentially underestimating their robustness. This behavior could arise from the increased uncertainties associated with the irradiation from multiple angles in PAT, compared to the more limited number of directions used in IMPT for glioma patients.

5.2.3. Scenario-based Robustness Evaluation

In addition to the voxelwise metrics used for the robustness evaluation of the plans, a scenario-based evaluation was also performed. More specifically, the 28 scenarios of each plan were combined across the patient population in order to assess whether they comply with the clinical goal.

For the $V_{95\%}$, the performances of the clinical, 9-, 18-, and 27-directions plans were similar, with no significant statistical differences. These plans outperformed the others, more specifically the 6-directions plan and those using range shifters, which exhibited lower median values, greater spread, and more scenarios where the clinical goal was not achieved.

In both the 28 evaluation scenarios and the voxelwise maximum, the clinical plan performed the best in terms of the $D_{2\%}$. Regarding the PAT plans, their performances were inferior to the clinical plan in the voxelwise maximum assessment, with several values exceeding the clinical goal. However, in the scenario-based evaluation, all PAT plans met the clinical goal, with none exceeding it.

In the evaluation of the $D_{98\%}$, the clinical plan once again performed the best, achieving the highest median value. However, all plans, except for the 18-directions one, included scenarios where the clinical goal was not met.

5.3. LET and RBE distributions

5.3.1. Intersection of the Healthy Brain Volume with the 60% Prescribed Dose Isodose Volume

For the intersection of the 60% prescribed dose isodose volume with the healthy brain volume, the plans using the range shifter outperformed all other plans in most intersection volumes, except for the 10 cc volume, showing the lowest median LET_d values and a generally moderate spread. This outcome could be attributed to the interaction of protons with the range shifter material, which modifies the energy spectrum of the beam. Specifically, the range shifter reduces the maximum proton energy, which in turn mitigates hotspots of high LET_d. The 6-directions plan performed the worst among all PAT plans, with the highest median LET_d values, followed by the 27-directions plan in the two lower volumes. However, the performance of the 27-directions plan improved in the two larger volumes, where it showed the lowest median value in the 10 cc overlap. The plans with 9- and 18-directions demonstrated relatively consistent performance across all volumes.

5.3.2. Intersection of the Healthy Brain Volume with the 90% Prescribed Dose Isodose Volume

For the intersection of the 90% prescribed dose isodose volume with the healthy brain volume, the clinical plan generally performed the worst, exhibiting the highest median LET_d values, although with a smaller spread compared to most of the PAT plans across the different volumes. The best performance in the two smaller volumes was achieved by the 18-directions plan with the range shifter, which maintained a consistently high rank in the larger two volumes, despite exhibiting a large spread. However, in these larger volumes, the 27-directions plan outperformed the 18-directions plan, similar to the results observed with the 60% prescribed dose isodose volume. Once again, the 6-directions plan demonstrated the worst performance among the PAT plans, exhibiting high median LET_d values similar to those of the clinical plan.

5.3.3. General Remarks

Overall, having the lowest median LET_d values are desirable, since the overlap volume refers to a part of the healthy brain volume in the high dose region. In general, the clinical plans perform poorly, exhibiting high median LET_d values similar to those of the 6-directions plans. In most cases, the plans that incorporate a range shifter perform the best, with the 9-, 18-, and 27-directions plans also showing relatively strong outcomes. It is important to note that, while using a 0.03 cc intersection volume is a common practice, especially when evaluating the LET_d values of OARs such as the brainstem and optic system, it is still a small volume that may not accurately reflect the performance of the plans in the LET analysis. The same applies to the 0.1 cc volumes, while the 1 and 10 cc volumes should be considered more reliable. Overall, the analysis reveals that in areas with larger intersection volumes, the LET_d values decrease. This is logical given the cumulative nature of a typical LVH, as seen in Figure 3.3.

5.3.4. Effective RBE

The effective RBE values for the brainstem core and surface showed that the plans incorporating a range shifter had the lowest median effective RBE values with the lowest spread, while the plans with the 18-directions had the highest median values. For the optic system, specifically the optic chiasma and both optic nerves, the clinical plan performed the worst, exhibiting the highest median effective RBE values, while the other plans showed relatively similar results. However, for the right optic nerve, the plans with the range shifter again outperformed the others.

The highest median effective RBE values are seen in the brainstem core, which signifies that in this OAR the LET values are higher causing the possibility of brainstem necrosis.

6

Conclusion

From the beginning of this project, it was clear that the research in PAT for neuro-oncological patients would lead to longer treatment times. However, if this approach aligned with literature indicating that PAT plans are more robust than IMPT plans, the drawback of extended treatment times could be somewhat mitigated. The findings presented earlier though, do not support this expectation. Specifically, the clinical plan surpasses the PAT plans in both robustness evaluation methods: voxelwise metrics analysis and scenario-based evaluation. Although the PAT plans satisfy the clinical goals in the scenario-based evaluation, the clinical plan demonstrates a distinct and notable advantage, highlighting the need for more advanced robustness evaluation approaches for PAT.

As far as the LET analysis is concerned, the first results are encouraging with the PAT plans showing lower median LET_d values compared to the clinical plan. Among them, the PAT plans including a range shifter tend to perform the best. Given that the clinical plan also incorporates a range shifter, this suggests that adding more beam directions helps reduce the LET_d values. It is also important to note that, although the clinical plan is designed with beam angles more than 90 degrees apart to minimize the risk of high LET_d buildup regions, the PAT plans still appear to perform better. In the effective RBE analysis, a high effective RBE indicates the accumulation of elevated LET_d values. The plans with a range shifter demonstrate superior performance across nearly all evaluated OARs, consistent with their observed reduction in the LET_d values.

The rationale for introducing the range shifter is to determine whether it enhances the outcomes in PAT. While the LET analysis indicates favorable results for PAT plans with a range shifter, these plans were generally far less robust than the other PAT plans based on both robustness evaluation methods. Deciding whether to advocate for their use requires weighing a critical trade-off: should one prioritize reducing LET_d values at the cost of robustness, or favor robustness at the expense of lower LET_d values?

An important point to consider from the conclusions drawn is that the PAT plans developed and analyzed in this project are based on a step-and-shoot approach rather than dynamic techniques. This limitation arises from the capabilities of the machinery available at HollandPTC. As a result, several aspects of this analysis, including

treatment efficiency, may differ compared to what could be achieved with dynamic methods. In this context, adopting a dynamic approach could potentially reduce treatment time further, with additional implications for the other two aspects evaluated in this study.

In summary, the study of PAT for glioma patients revealed promising outcomes in the LET analysis, though it also highlighted longer treatment durations and reduced robustness based on current evaluation methods. Utilizing more advanced optimization techniques could further enhance the performance of PAT plans in LET/RBE analysis, while improved evaluation methods may reveal more favorable robustness results for PAT plans.

Bibliography

[1] Radhe Mohan. A review of proton therapy–current status and future directions. *Precision radiation oncology*, 6(2):164–176, 2022.

[2] Radhe Mohan and David Grosshans. Proton therapy–present and future. *Advanced drug delivery reviews*, 109:26–44, 2017.

[3] Mary Elizabeth Davis. Epidemiology and overview of gliomas. In *Seminars in oncology nursing*, volume 34, pages 420–429. Elsevier, 2018.

[4] Mario Caccese, Marta Padovan, Domenico D'Avella, Franco Chioffi, Marina Paola Gardiman, Franco Berti, Fabio Busato, Luisa Bellu, Eleonora Bergo, Marco Zoccarato, et al. Anaplastic astrocytoma: state of the art and future directions. *Critical Reviews in Oncology/Hematology*, 153:103062, 2020.

[5] Laszlo Mechtler. Neuroimaging in neuro-oncology. *Neurologic clinics*, 27(1):171–201, 2009.

[6] Marion Smits. Imaging of oligodendroglioma. *The British journal of radiology*, 89(1060):20150857, 2016.

[7] Naomi Morita, Sumei Wang, Sanjeev Chawla, Harish Poptani, and Elias R Melhem. Dynamic susceptibility contrast perfusion weighted imaging in grading of nonenhancing astrocytomas. *Journal of Magnetic Resonance Imaging*, 32(4):803–808, 2010.

[8] Jaymin Jhaveri, En Cheng, Sibo Tian, Zachary Buchwald, Mudit Chowdhary, Yuan Liu, Theresa W Gillespie, Jeffrey J Olson, Aidnag Z Diaz, Alfredo Voloschin, et al. Proton vs. photon radiation therapy for primary gliomas: an analysis of the national cancer data base. *Frontiers in oncology*, 8:440, 2018.

[9] Eudocia C Quant, Andrew D Norden, Jan Drappatz, Alona Muzikansky, Lisa Doherty, Debra LaFrankie, Abigail Ciampa, Santosh Kesari, and Patrick Y Wen. Role of a second chemotherapy in recurrent malignant glioma patients who progress on bevacizumab. *Neuro-oncology*, 11(5):550–555, 2009.

[10] Stephen P Jackson. Sensing and repairing dna double-strand breaks. *Carcinogenesis*, 23(5):687–696, 2002.

[11] Theresa A Lawrie, David Gillespie, Therese Dowswell, Jonathan Evans, Sara Erridge, Luke Vale, Ashleigh Kernohan, and Robin Grant. Long-term neurocognitive and other side effects of radiotherapy, with or without chemotherapy, for glioma. *Cochrane Database of Systematic Reviews*, (8), 2019.

[12] Isabelle Chambrelant, Jordan Eber, Delphine Antoni, Hélène Burckel, Georges Noël, and Romane Auvergne. Proton therapy and gliomas: a systematic review. *Radiation*, 1(3):218–233, 2021.

[13] Jonathan B Farr, Jacob B Flanz, Alexander Gerbershagen, and Michael F Moyers. New horizons in particle therapy systems. *Medical physics*, 45(11):e953–e983, 2018.

[14] Xuanfeng Ding, Xiaoqiang Li, An Qin, Jun Zhou, Di Yan, Peter Chen, Chinnaiyan Prakash, Craig Stevens, Rohan Deraniyagala, and Peyman Kabolizadeh. Redefine the role of range shifter in treating bilateral head and neck cancer in the era of intensity modulated proton therapy. *Journal of applied clinical medical physics*, 19(5):749, 2018.

[15] Jasika Paramasamy. Impact of variations in patient and beam parameters on proton therapy using pencil beam scanning technique. 2022.

[16] Daniel Sánchez-Parcerisa, JC Pourbaix, CG Ainsley, D Dolney, and A Carabe. Fast range switching of passively scattered proton beams using a modulation wheel and dynamic beam current modulation. *Physics in Medicine & Biology*, 59(7):N19, 2014.

[17] Hanne M Kooy, Benjamin M Clasie, Hsiao-Ming Lu, Thomas M Madden, Hassan Bentefour, Nicolas Depauw, Judy A Adams, Alexei V Trofimov, Denis Demaret, Thomas F Delaney, et al. A case study in proton pencil-beam scanning delivery. *International Journal of Radiation Oncology* Biology* Physics*, 76(2):624–630, 2010.

[18] Stewart Mein, Sophie Wuyckens, Xiaoqiang Li, Stefan Both, Alejandro Carabe, Macarena Chocan Vera, Erik Engwall, Fracchiolla Francesco, Christian Graeff, Wenbo Gu, et al. Particle arc therapy: Status and potential. *Radiotherapy and Oncology*, page 110434, 2024.

[19] Erik Engwall, Otte Marthin, Viktor Wase, Johan Sundström, Victor Mikhalev, Bas A de Jong, Johannes A Langendijk, Henrik Melbéus, Björn Andersson, Erik W Korevaar, et al. Partitioning of discrete proton arcs into interlaced subplans can bring proton arc advances to existing proton facilities. *Medical Physics*, 50(9):5723–5733, 2023.

[20] Jonathan T Whaley, Maura Kirk, Keith Cengel, James McDonough, Justin Bekelman, and John P Christodouleas. Protective effect of transparent film dressing on proton therapy induced skin reactions. *Radiation Oncology*, 8:1–6, 2013.

[21] Laura Toussaint, Daniel J Indelicato, Katrine S Holgersen, Jørgen BB Petersen, Camilla H Stokkevåg, Yasmin Lassen-Ramshad, Oscar Casares-Magaz, Anne Vestergaard, and Ludvig P Muren. Towards proton arc therapy: physical and biologically equivalent doses with increasing number of beams in pediatric brain irradiation. *Acta oncologica*, 58(10):1451–1456, 2019.

[22] Serena Psoroulas, Christian Bula, Oxana Actis, Damien Charles Weber, and David Meer. A predictive algorithm for spot position corrections after fast energy

switching in proton pencil beam scanning. *Medical physics*, 45(11):4806–4815, 2018.

[23] Gang Liu, L Zhao, W Zheng, A Qin, D Yan, G Janssens, J Shen, C Stevens, P Kabolizadeh, and X Ding. Develop an accurate model of spot-scanning treatment delivery time for a compact superconducting synchrocyclotron proton system. In *MEDICAL PHYSICS*, volume 47, pages E741–E741. WILEY 111 RIVER ST, HOBOKEN 07030-5774, NJ USA, 2020.

[24] Ulrich W Langner, John G Eley, Lei Dong, and Katja Langen. Comparison of multi-institutional varian probeam pencil beam scanning proton beam commissioning data. *Journal of applied clinical medical physics*, 18(3):96–107, 2017.

[25] T Inaniwa, H Tashima, and N Kanematsu. Optimum size of a calibration phantom for x-ray ct to convert the hounsfield units to stopping power ratios in charged particle therapy treatment planning. *Journal of Radiation Research*, 59(2):216–224, 2018.

[26] Wei Liu, Xiaodong Zhang, Yupeng Li, and Radhe Mohan. Robust optimization of intensity modulated proton therapy. *Medical physics*, 39(2):1079–1091, 2012.

[27] Macarena S Chocan, Sophie Wuyckens, Damien Dasnoy, Dario Di Perri, Elena Borderias Villarruel, Erik Engwall, John A Lee, Ana M Barragán-Montero, and Edmond Sterpin. A dosimetric and robustness analysis of proton arc therapy with early energy layer and spot assignment for lung cancer versus conventional intensity modulated proton therapy. *Acta Oncologica*, 63:40549, 2024.

[28] Jan Unkelbach and Harald Paganetti. Robust proton treatment planning: physical and biological optimization. In *Seminars in radiation oncology*, volume 28, pages 88–96. Elsevier, 2018.

[29] Erik W Korevaar, Steven JM Habraken, Daniel Scandurra, Roel GJ Kierkels, Mirko Unipan, Martijn GC Eenink, Roel JHM Steenbakkers, Stephanie G Peeters, Jaap D Zindler, Mischa Hoogeman, et al. Practical robustness evaluation in radiotherapy–a photon and proton-proof alternative to ptv-based plan evaluation. *Radiotherapy and Oncology*, 141:267–274, 2019.

[30] Albin Fredriksson and Rasmus Bokrantz. A critical evaluation of worst case optimization methods for robust intensity-modulated proton therapy planning. *Medical physics*, 41(8Part1):081701, 2014.

[31] Fada Guan, Christopher Peeler, Lawrence Bronk, Changran Geng, Reza Taleei, Sharmalee Randeniya, Shuaiping Ge, Dragan Mirkovic, David Grosshans, Radhe Mohan, et al. Analysis of the track-and dose-averaged let and let spectra in proton therapy using the geant4 monte carlo code. *Medical physics*, 42(11):6234–6247, 2015.

[32] Edward AK Smith, Carla Winterhalter, Tracy SA Underwood, Adam H Aitkenhead, Jenny C Richardson, Michael J Merchant, Norman F Kirkby, Karen J Kirby, and Ranald I Mackay. A monte carlo study of different let definitions and calculation

parameters for proton beam therapy. *Biomedical Physics & Engineering Express*, 8(1):015024, 2021.

[33] Daphne Haas-Kogan, Daniel Indelicato, Harald Paganetti, Natia Esiashvili, Anita Mahajan, Torunn Yock, Stella Flampouri, Shannon MacDonald, Maryam Fouladi, Kry Stephen, et al. National cancer institute workshop on proton therapy for children: considerations regarding brainstem injury. *International Journal of Radiation Oncology* Biology* Physics*, 101(1):152–168, 2018.

[34] Christian P Karger and Peter Peschke. Rbe and related modeling in carbon-ion therapy. *Physics in Medicine & Biology*, 63(1):01TR02, 2017.

[35] Fada Guan, Lawrence Bronk, Uwe Titt, Steven H Lin, Dragan Mirkovic, Matthew D Kerr, X Ronald Zhu, Jeffrey Dinh, Mary Sobieski, Clifford Stephan, et al. Spatial mapping of the biologic effectiveness of scanned particle beams: towards biologically optimized particle therapy. *Scientific reports*, 5(1):9850, 2015.

[36] Christopher R Peeler, Dragan Mirkovic, Uwe Titt, Pierre Blanchard, Jillian R Gunther, Anita Mahajan, Radhe Mohan, and David R Grosshans. Clinical evidence of variable proton biological effectiveness in pediatric patients treated for ependymoma. *Radiotherapy and Oncology*, 121(3):395–401, 2016.

[37] Eivind Rørvik, Lars Fredrik Fjæra, Tordis J Dahle, Jon Espen Dale, Grete May Engeseth, Camilla H Stokkevåg, Sara Thörnqvist, and Kristian S Ytre-Hauge. Exploration and application of phenomenological rbe models for proton therapy. *Physics in Medicine & Biology*, 63(18):185013, 2018.

[38] Andries N Schreuder, Daniel S Bridges, Lauren Rigsby, Marc Blakey, Martin Janson, Samantha G Hedrick, and John B Wilkinson. Validation of the raystation monte carlo dose calculation algorithm using realistic animal tissue phantoms. *Journal of Applied Clinical Medical Physics*, 20(10):160–171, 2019.

[39] Kees Spruijt, Sina Mossahebi, Haibo Lin, Eunsin Lee, James Kraus, Anees Dhabaan, Per Poulsen, Matthew Lowe, Ahmet Ayan, Sylvie Spiessens, et al. Multi-institutional consensus on machine qa for isochronous cyclotron-based systems delivering ultra-high dose rate (flash) pencil beam scanning proton therapy in transmission mode. *Medical Physics*, 51(2):786–798, 2024.

[40] Hao Gao, Benjamin Clasie, Mark McDonald, Katja M Langen, Tian Liu, and Yuting Lin. Plan-delivery-time constrained inverse optimization method with minimum-mu-per-energy-layer (mmpel) for efficient pencil beam scanning proton therapy. *Medical Physics*, 47(9):3892–3897, 2020.
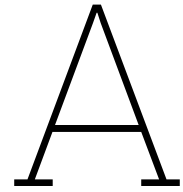
Scripting

A.1. Delivery Time Calculation

A.1.1. PAT Plans

```python
"""
from connect import *
import math
import numpy as np
from dose_rate_config import DR_lookup_table
from datetime import timedelta
import os
import json

def get_spot_weights(segment, beamMU):
    """Get the spot weights for the given segment"""
    result = []
    for weight in segment.Spots.Weights:
        result.append(weight*beamMU)
    return result

def get_spot_positions(segment):
    """Get the spot positions for the given segment"""
    result = []
    for position in segment.Spots.Positions:
        result.append(position)
    return result


def get_spot_delivery_time(spotMU, energy):
    """Calculate the spot delivery times"""
    result = []
    print(f'List spot MU of energy {energy}: {spotMU}')
    min_MU = min(spotMU)
    print(f'Min MU in energy layer: {min_MU}')
    energies, dose_rates = np.transpose(DR_lookup_table)
    max_DR = np.interp(energy, energies, dose_rates) # dose rate in MU/s
    cal_DR = 21000*min_MU/60
    if cal_DR > max_DR:
        DR = max_DR
```

```python
36      else:
37          DR = cal_DR
38      print(f'max DR = {max_DR}, cal DR = {cal_DR}')
39      for MU in spotMU:
40          time = MU/DR*1000 # ms
41          result.append(time)
42          min_time = max(result)
43          print(f'MU: {MU}, time: {time}')
44      print(f'Max time: {min_time}')
45      return result
46
47
48  def get_spot_off_time(spotPos):
49      """Calculate the time required to move to the next spot"""
50      speedX = 500 # cm/s
51      speedY = 2000 # cm/s
52      result = []
53      for i in range(1, len(spotPos)):
54          dx = spotPos[i]['x']-spotPos[i-1]['x']
55          dy = spotPos[i]['y']-spotPos[i-1]['y']
56          timeX = abs(dx)/speedX
57          timeY = abs(dy)/speedY
58          time = max(timeX, timeY)*1000 # ms
59          result.append(time)
60      return result
61
62  def get_beam_switch_time(beamInfo):
63      """Calculate the time required to switch between beam angles"""
64      acceleration = 2 # max º/s²
65      speed = 6 # max º/s
66      result = []
67      acceleration_distance = 0.5*speed**2/acceleration # º
68      acceleration_time = speed/acceleration # s
69      for i in range(1, len(beamInfo[0]['SegmentAngles'])):
70          dAngle = abs(beamInfo[0]['SegmentAngles'][i] - beamInfo[0]['
                  SegmentAngles'][i-1])
71          if dAngle == 0:
72              beamSwitch = 0 # ms
73          elif dAngle >= acceleration_distance:
74              beamSwitch = ((dAngle - acceleration_distance)/speed +
                      acceleration_time)*1000 # ms
75              beamSwitch += 45000 # Add extra 45s to prepare new beam
76          else:
77              beamSwitch = np.sqrt(2*(dAngle/acceleration))*1000 # ms
78              beamSwitch += 45000 # Add extra 45s to prepare new beam
79          result.append(beamSwitch)
80      return result
81
82  def get_delivery_timeline(planInfo, patientID, patientPlan):
83      BeamSwitchTime = get_beam_switch_time(planInfo)
84      num = 0
85      start_time = 0
86      treatment_record = {}
87      treatment_record['_comment'] = f'Treatment record file for {patientID}
                  | {patientPlan}'
88      treatment_record['beam'] = []
```

```python
89
90      all_spot_delivery_times = []
91
92      for i in range(len(planInfo)):
93          beam_dict = {'beamname': planInfo[i]['BeamName'],
94                       'layer': []}
95          for j in range(len(planInfo[i]['Energies'])):
96              print(f"Energy: {planInfo[i]['Energies'][j]}")
97              spot_dict = {'spot': [{'start': start_time}]}
98              for k in range(len(planInfo[i]['SpotDeliveryTime'][j])):
99                  spot_time = planInfo[i]['SpotDeliveryTime'][j][k]
100                 all_spot_delivery_times.append(spot_time)
101                 start_time += spot_time
102                 if k != len(planInfo[i]['SpotDeliveryTime'][j])-1:
103                     off_time = planInfo[i]['SpotOffTime'][j][k]
104                     start_time += off_time
105                     spot_dict['spot'].append({'start': start_time})
106
107             if j != len(planInfo[i]['Energies'])-1 and BeamSwitchTime[j]
                    == 0:
108                 print('Switch energy')
109                 start_time += 780 # energy switching time ms
110             elif j != len(planInfo[i]['Energies'])-1 and BeamSwitchTime[j]
                    != 0:
111                 print('Switch beam angle')
112                 start_time += BeamSwitchTime[j] # add beam switch time
113             beam_dict['layer'].append(spot_dict)
114         treatment_record['beam'].append(beam_dict)
115
116
117     max_spot_delivery_time = max(all_spot_delivery_times)
118     print(f'The maximum spot delivery time in the entire plan  is: {
            max_spot_delivery_time}')
119
120     return treatment_record, start_time
121
122 Patient = get_current('Patient')
123 PatientID = Patient.PatientID
124 Plan = get_current('Plan')
125 PatientPlan = Plan.Name
126 BeamSet = get_current('BeamSet')
127
128 plan_info = {}
129
130 for idx, Beam in enumerate(BeamSet.Beams):
131     Energies = []
132     SegmentAngles = []
133     SpotWeights = []
134     SpotPositions = []
135     SpotDeliveryTime = []
136     SpotOffTime = []
137     BeamName = Beam.Name
138     BeamMU = Beam.BeamMU
139     BeamAngle = Beam.GantryAngle
140     for Segment in Beam.Segments:
141         SpotPos = []
```

```python
142            NominalEnergy = Segment.NominalEnergy
143            Energies.append(NominalEnergy)
144            SegmentAngle = BeamAngle + Segment.IonArcSegmentProperties.
                   DeltaGantryAngle
145            SegmentAngles.append(SegmentAngle)
146            SpotMU = get_spot_weights(Segment, BeamMU)
147            SpotPos = get_spot_positions(Segment)
148            SpotDelivery = get_spot_delivery_time(SpotMU, NominalEnergy)
149            SpotOff = get_spot_off_time(SpotPos)
150            SpotWeights.append(SpotMU)
151            SpotPositions.append(SpotPos)
152            SpotDeliveryTime.append(SpotDelivery)
153            SpotOffTime.append(SpotOff)
154        plan_info[idx] = {'BeamName': BeamName,
155                          'BeamAngle': BeamAngle,
156                          'Energies': Energies,
157                          'SegmentAngles': SegmentAngles,
158                          'SpotWeights': SpotWeights,
159                          'SpotPositions': SpotPositions,
160                          'SpotDeliveryTime': SpotDeliveryTime,
161                          'SpotOffTime': SpotOffTime
162                          }
163
164 treatment_record, treatment_time = get_delivery_timeline(plan_info,
        PatientID, PatientPlan)
165
166 print(f'Treatment time is {treatment_time/1000} s')
167
168 def convert_time(seconds):
169     # Calculate hours
170     hours = seconds // 3600
171     seconds %= 3600
172     # Calculate minutes
173     minutes = seconds // 60
174     seconds %= 60
175     # Calculate seconds and milliseconds
176     secs = int(seconds)
177     milliseconds = round((seconds - secs) * 1000)
178     return f"{hours}h {minutes}m {secs}s {milliseconds}ms"
179
180 formatted_time = convert_time(treatment_time/1000)
181 print(formatted_time)
182 print("")
183
184 path = "H:\\Pelagia\\"+PatientID
185 if os.path.exists(path):
186     print("Directory already exists")
187     print("")
188 else:
189     os.mkdir(path)
190
191 folder = "H:\\Pelagia\\"+PatientID+"\\"+PatientPlan+".json"
192 with open(folder, 'w') as outfile:
193     json.dump(treatment_record, outfile, indent=4)
194 print('Json file generated')
```

A.1.2. Clinical Plan

To calculate the delivery time for the clinical plans, the same script was used as above, with some adjustments to the beam switching time. This change was necessary because the PAT plans utilized a single beam with multiple arc directions, whereas the clinical plan involved three separate beam directions.

```python
"""
def get_beam_switch_time(beamInfo):
    """Calculate the time required to switch between beam angles"""
    acceleration = 2 # max º/s²
    speed = 6 # max º/s
    result = []
    acceleration_distance = 0.5*speed**2/acceleration # º
    acceleration_time = speed/acceleration # s
    for i in range(1, len(beamInfo)):
        dAngle = abs(beamInfo[i]['BeamAngle'] - beamInfo[i-1]['BeamAngle'])
        if dAngle >= acceleration_distance:
            beamSwitch = ((dAngle - acceleration_distance)/speed +
                acceleration_time)*1000 # ms
        else:
            beamSwitch = np.sqrt(2*(dAngle/acceleration))*1000 # ms
            beamSwitch += 45000 # Add extra 45s to prepare new beam
        result.append(beamSwitch)
    return result
```

B

Delivery Time

B.0.1. Delivery Time Components per Plan, for All Patients
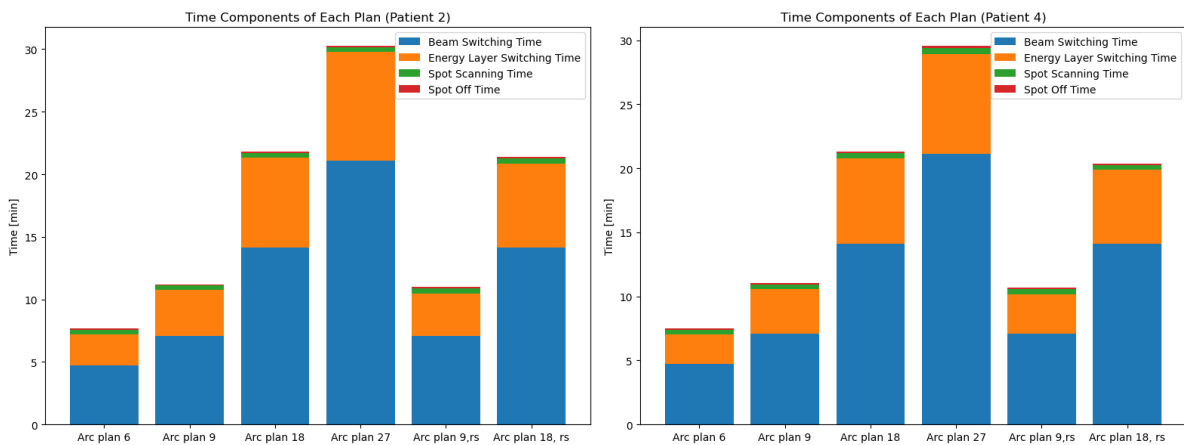
Figure B.1: The delivery time components [min] per PAT plan, for patient 2 in the left figure and 4 in the right.
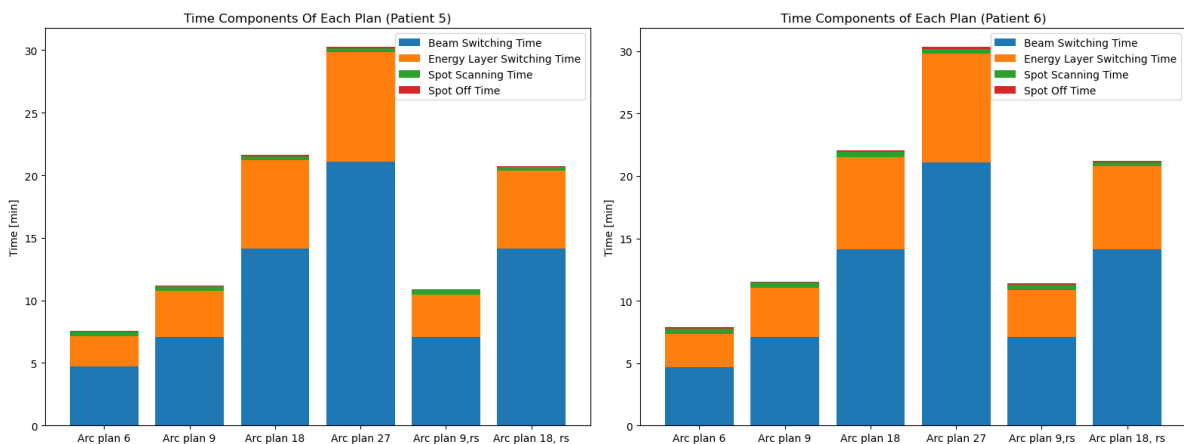
Figure B.2: The delivery time components [min] per PAT plan, for patient 5 in the left figure and 6 in the right.
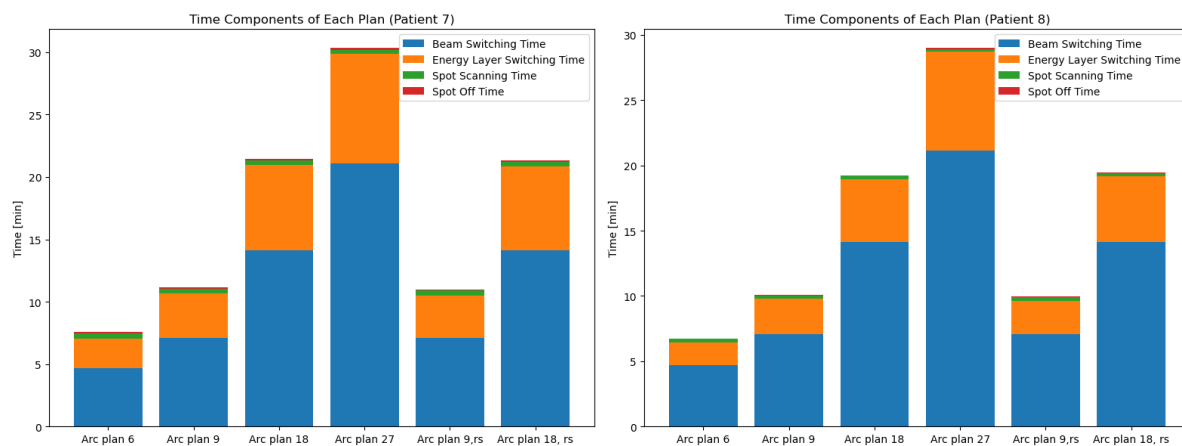
Figure B.3: The delivery time components [min] per PAT plan, for patient 7 in the left figure and 8 in the right.
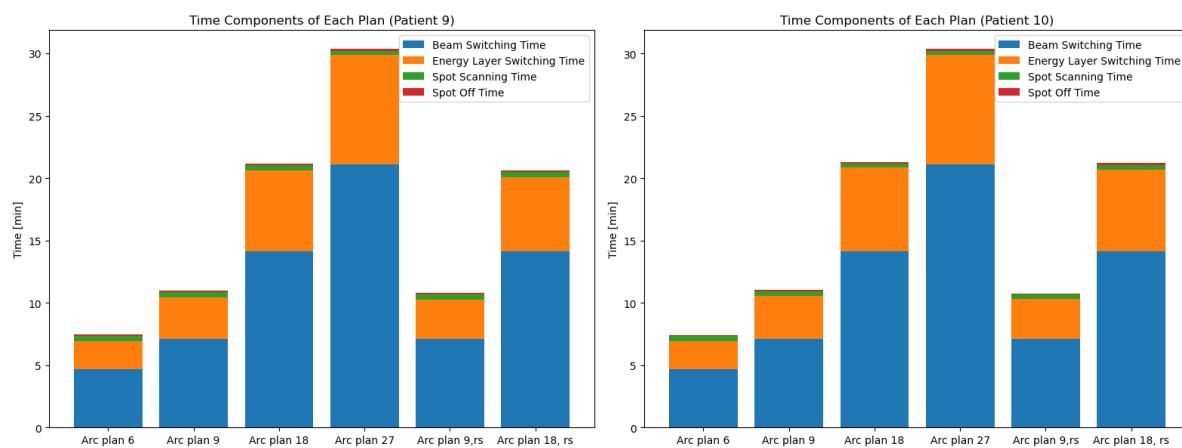
Figure B.4: The delivery time components [min] per PAT plan, for patient 9 in the left figure and 10 in the right.
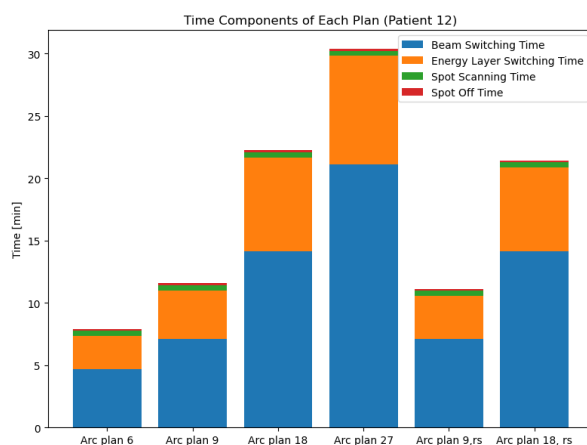
Figure B.5: The delivery time components [min] per PAT plan, for patient 12.

C
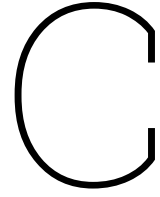
Robustness

C.0.1. Tables of the Nominal and Voxelwise $V_{95\%}$, $D_{2\%}$ and $D_{98\%}$ Values

Table C.1: Median, minimum, and maximum $V_{95\%}$ [%] for each plan across the patient population in the nominal scenario. The table also includes the IQR as a measure of data dispersion.

Plan	Median	Minimum	Maximum	IQR
Clinical	99.87	98.89	100	0.63
6 directions	99.83	98.57	100	0.5
9 directions	99.98	99.35	100	0.19
18 directions	99.89	99.55	100	0.31
27 directions	99.94	99.36	100	0.17
9 directions, range shifter	99.84	98.96	100	0.38
18 directions, range shifter	99.8	99.01	100	0.56

Table C.2: Median, minimum, and maximum voxelwise minimum $V_{95\%}$ [%] for each plan across the patient population. The table also includes the IQR as a measure of data dispersion.

Plan	Median	Minimum	Maximum	IQR
Clinical	98.92	97.52	99.88	1.45
6 directions	97.66	94.23	99.18	3.11
9 directions	98.3	94.97	98.87	1.31
18 directions	97.87	96.4	98.74	1.83
27 directions	97.48	94.77	98.45	2.09
9 directions, range shifter	97.06	94.85	98.5	2.04
18 directions, range shifter	96.82	93.15	98.39	3.31

Table C.3: Median, minimum, and maximum $D_{2\%}$ [Gy] for each plan across the patient population in the nominal scenario. The table also includes the IQR as a measure of data dispersion.

Plan	Median	Minimum	Maximum	IQR
Clinical	61.32	60.87	61.62	0.13
6 directions	62.12	61.96	63.02	0.21
9 directions	62.1	61.99	62.35	0.1
18 directions	61.86	61.7	62.09	0.18
27 directions	61.77	61.54	62.31	0.13
9 directions, range shifter	62	61.76	62.35	0.36
18 directions, range shifter	61.8	61.39	62.39	0.35

Table C.4: Median, minimum, and maximum voxelwise maximum $D_{2\%}$ [Gy] for each plan across the patient population. The table also includes the IQR as a measure of data dispersion.

Plan	Median	Minimum	Maximum	IQR
Clinical	62.22	61.62	62.41	0.2
6 directions	63.53	63.35	64.68	0.35
9 directions	63.52	63.34	63.84	0.15
18 directions	63.17	62.95	63.44	0.16
27 directions	63.1	62.67	64.16	0.1
9 directions, range shifter	63.55	62.97	63.93	0.43
18 directions, range shifter	63.24	62.42	63.95	0.82

Table C.5: Median, minimum, and maximum $D_{98\%}$ [Gy] for each plan across the patient population in the nominal scenario. The table also includes the IQR as a measure of data dispersion.

Plan	Median	Minimum	Maximum	IQR
Clinical	58.46	58.03	58.82	0.27
6 directions	58.12	57.2	58.56	0.46
9 directions	58.21	57.97	58.6	0.26
18 directions	58.14	57.5	58.5	0.24
27 directions	58.1	57.85	58.45	0.24
9 directions, range shifter	58.24	57.39	58.62	0.24
18 directions, range shifter	58.12	57.35	58.54	0.52

Table C.6: Median, minimum, and maximum voxelwise minimum $D_{98\%}$ [Gy] for each plan across the patient population. The table also includes the IQR as a measure of data dispersion.

Plan	Median	Minimum	Maximum	IQR
Clinical	57.08	55.69	57.98	0.99
6 directions	56.18	53.85	56.87	1.58
9 directions	56.52	54.77	56.75	0.84
18 directions	56.32	55.39	56.77	0.96
27 directions	56.06	54.71	56.65	1.04
9 directions, range shifter	55.72	54.37	56.79	1.45
18 directions, range shifter	55.58	53.96	56.63	1.86

C.0.2. Assessment of the Reliability of the Voxelwise Metrics in the Robustness Evaluation
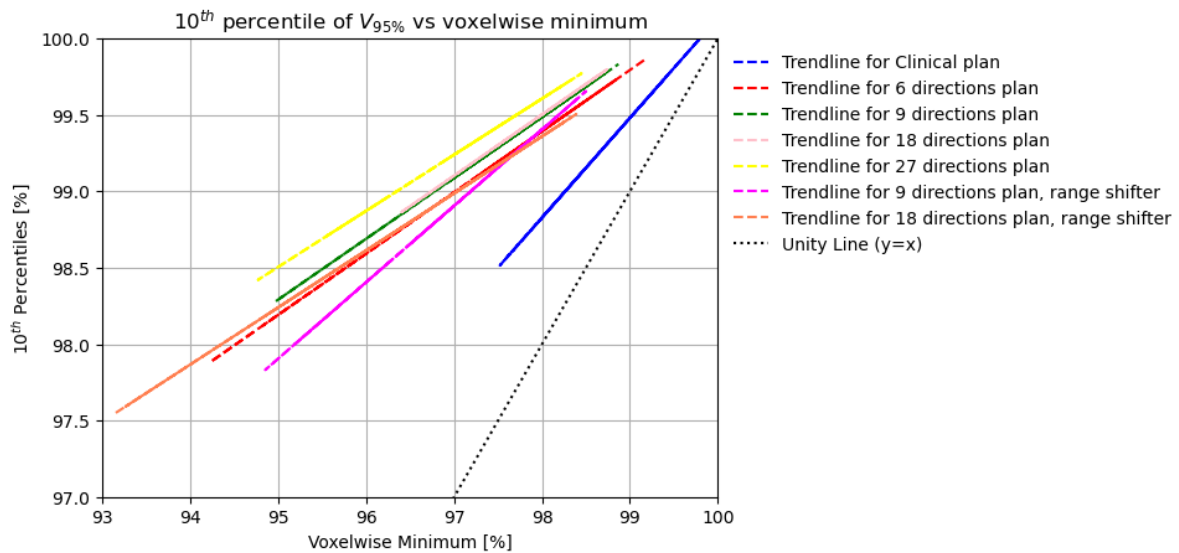
Figure C.1: 10th percentiles of the $V_{95\%}$ [%] based on the 28 evaluation scenarios of each patient across the whole population as a function of the voxelwise minimum.

Table C.7: Angular differences between the fitted lines of the 10th percentiles for the $V_{95\%}$ and the unity line.

Plan	Angular difference [○] with the unity line
Clinical	11.88
6 directions	23.18
9 directions	23.29
18 directions	23.23
27 directions	24.84
9 directions, range shifter	18.44
18 directions, range shifter	24.54
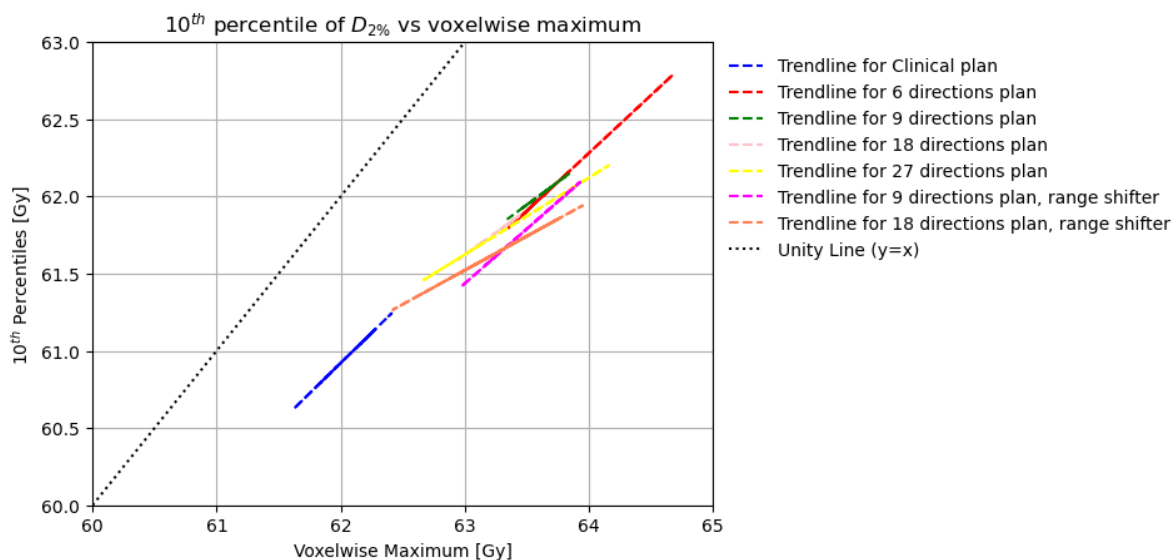
Figure C.2: 10th percentiles of the $D_{2\%}$ [Gy] based on the 28 evaluation scenarios of each patient across the whole population as a function of the voxelwise maximum.

Table C.8: Angular differences between the fitted lines of the 10th percentiles for the $D_{2\%}$ and the unity line.

Plan	Angular difference [○] with the unity line
Clinical	6.88
6 directions	8.20
9 directions	14.47
18 directions	14.90
27 directions	18.54
9 directions, range shifter	9.78
18 directions, range shifter	21.19
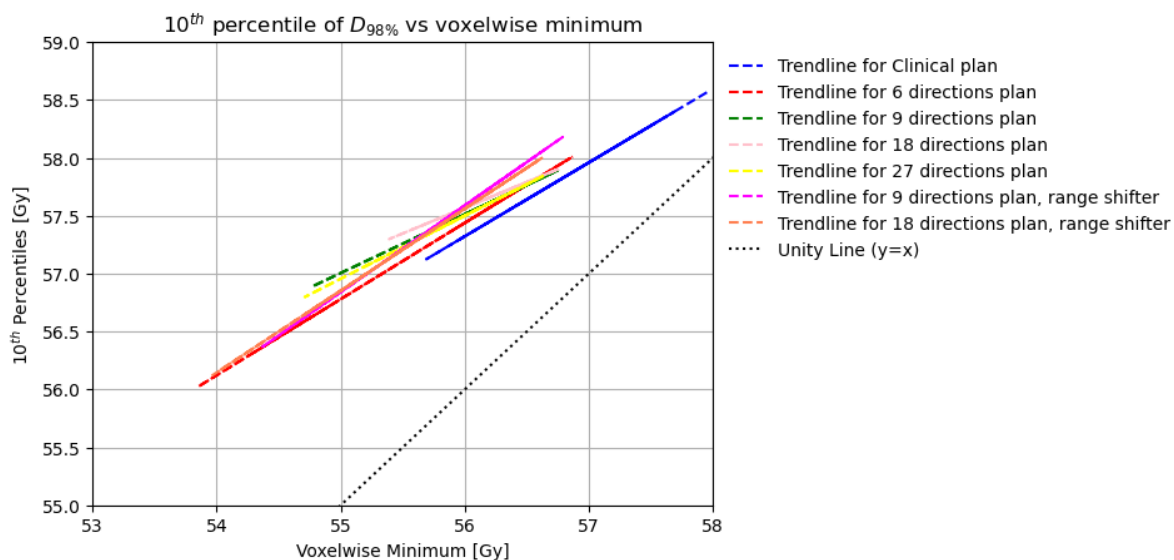
Figure C.3: 10th percentiles of the $D_{98\%}$ [Gy] based on the 28 evaluation scenarios of each patient across the whole population as a function of the voxelwise minimum.

Table C.9: Angular differences between the fitted lines of the 10th percentiles for the $D_{98\%}$ and the unity line.

Plan	Angular difference [○] with the unity line
Clinical	12.50
6 directions	11.65
9 directions	18.13
18 directions	21.08
27 directions	16.46
9 directions, range shifter	8.19
18 directions, range shifter	9.74

Linear Fitting of the 10th Percentile Points with the Voxelwise Minimum/Maximum across Different Plans and Metrics
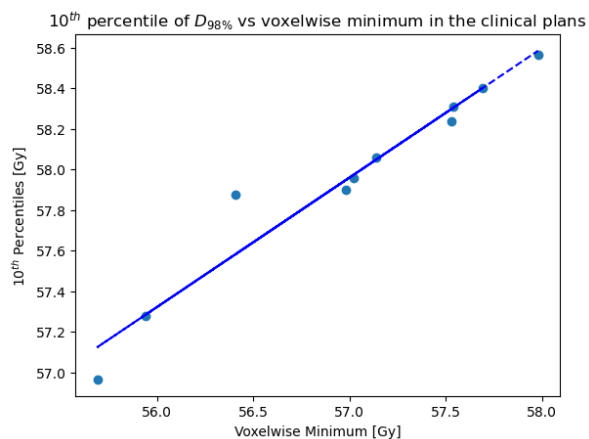
Figure C.4: The fitted line of the 10th percentiles for each patient as a function of the voxelwise minimum for the $D_{98\%}$ of the clinical plan.
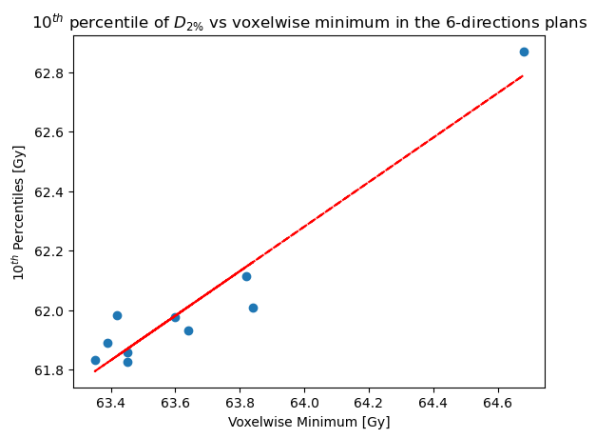
Figure C.5: The fitted line of the 10th percentiles for each patient as a function of the voxelwise minimum for the $D_{2\%}$ of the 6-directions plan.
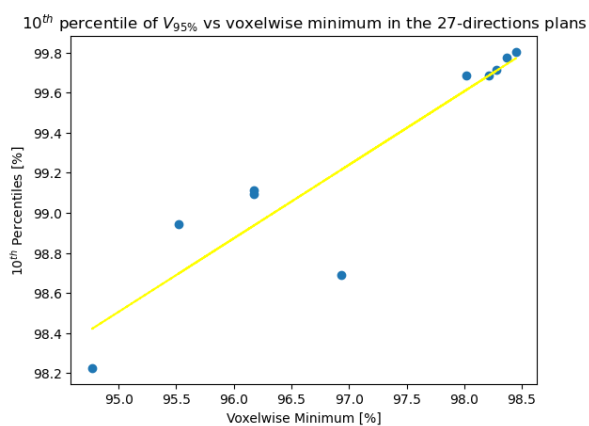
Figure C.6: The fitted line of the 10th percentiles for each patient as a function of the voxelwise minimum for the $V_{95\%}$ of the 27-directions plan.

C.0.3. Scenario-based Robustness Analysis

Table C.10: Median, minimum, and maximum $V_{95\%}$ [%] for the 28 scenarios of each plan across the patient population. The table also includes the IQR as a measure of data dispersion.

Plan	Median	Minimum	Maximum	IQR
Clinical	99.8	97.94	100	0.68
6 directions	99.68	97.24	100	0.77
9 directions	99.82	97.93	99.99	0.28
18 directions	99.75	98.44	100	0.43
27 directions	99.74	97.86	99.98	0.4
9 directions, range shifter	99.6	97.01	100	0.73
18 directions, range shifter	99.49	96.72	100	0.99

Table C.11: Median, minimum, and maximum $D_{2\%}$ [Gy] for the 28 scenarios of each plan across the patient population. The table also includes the IQR as a measure of data dispersion.

Plan	Median	Minimum	Maximum	IQR
Clinical	61.28	60.52	61.9	0.35
6 directions	62.23	61.71	63.54	0.38
9 directions	62.2	61.81	62.8	0.29
18 directions	61.93	61.56	62.36	0.26
27 directions	61.91	61.42	63.03	0.35
9 directions, range shifter	62.02	61.41	62.78	0.45
18 directions, range shifter	61.78	61.27	62.73	0.52

Table C.12: Median, minimum, and maximum $D_{98\%}$ [Gy] for the 28 scenarios of each plan across the patient population. The table also includes the IQR as a measure of data dispersion.

Plan	Median	Minimum	Maximum	IQR
Clinical	58.28	56.33	59.02	0.41
6 directions	57.9	55.04	58.4	0.62
9 directions	57.95	56.35	58.42	0.41
18 directions	57.92	57.06	58.31	0.31
27 directions	57.82	56.2	58.33	0.43
9 directions, range shifter	57.96	55.38	58.58	0.53
18 directions, range shifter	57.82	54.89	58.52	0.87

D

LET and RBE distributions

D.0.1. Tables of the LET_d Values for the Overlap Volumes of Interest

Table D.1: Median, minimum and maximum LET_d across all patient population for a 0.03 cc volume of the overlap structure (60% prescribed dose isodose volume). The table also includes the IQR as a measure of data dispersion.

Plan	Median	Minimum	Maximum	IQR
Clinical	6.19	5.74	7.17	0.78
6 directions	6.4	5.5	7.37	1.14
9 directions	5.95	4.72	7.31	1.24
18 directions	6.06	5.34	7.85	0.87
27 directions	6.18	3.93	7.73	1.94
9 directions, range shifter	5.72	4.69	6.75	1.17
18 directions, range shifter	5.38	3.77	6.91	0.92

Table D.2: Median, minimum and maximum LET_d across all patient population for a 0.1 cc volume of the overlap structure (60% prescribed dose isodose volume). The table also includes the IQR as a measure of data dispersion.

Plan	Median	Minimum	Maximum	IQR
Clinical	6.02	5.58	6.92	0.8
6 directions	6.16	5.29	6.95	0.88
9 directions	5.74	4.62	7.05	1.25
18 directions	5.68	5.21	7.49	0.58
27 directions	5.78	4.86	7.23	1.17
9 directions, range shifter	5.48	4.62	6.46	1.1
18 directions, range shifter	5.24	3.75	6.75	0.78

Table D.3: Median, minimum and maximum LET_d across all patient population for a 1 cc volume of the overlap structure (60% prescribed dose isodose volume). The table also includes the IQR as a measure of data dispersion.

Plan	Median	Minimum	Maximum	IQR
Clinical	5.62	5.08	6.33	0.74
6 directions	5.51	4.75	6.22	0.74
9 directions	5.1	4.31	6.28	0.85
18 directions	5.18	4.7	6.63	0.52
27 directions	5.14	4.44	6.57	0.62
9 directions, range shifter	5.07	4.07	5.76	0.71
18 directions, range shifter	4.88	3.62	5.95	0.82

Table D.4: Median, minimum and maximum LET_d across all patient population for a 10 cc volume of the overlap structure (60% prescribed dose isodose volume). The table also includes the IQR as a measure of data dispersion.

Plan	Median	Minimum	Maximum	IQR
Clinical	4.8	4.28	5.34	0.58
6 directions	4.62	3.78	5.04	0.45
9 directions	4.33	3.84	4.98	0.66
18 directions	4.39	3.93	5.24	0.3
27 directions	4.28	3.9	5.53	0.31
9 directions, range shifter	4.34	3.51	4.7	0.52
18 directions, range shifter	4.32	3.32	4.83	0.76

Table D.5: Median, minimum and maximum LET_d across all patient population for a 0.03 cc volume of the overlap structure (90% prescribed dose isodose volume). The table also includes the IQR as a measure of data dispersion.

Plan	Median	Minimum	Maximum	IQR
Clinical	4.94	4.73	5.68	0.61
6 directions	4.96	4.61	6.19	0.8
9 directions	4.86	4.12	6.43	1.14
18 directions	4.88	4.37	6.43	0.46
27 directions	4.94	4.23	6.46	1.17
9 directions, range shifter	4.86	4.08	5.44	0.78
18 directions, range shifter	4.54	3.53	5.76	0.94

Table D.6: Median, minimum and maximum LET$_d$ across all patient population for a 0.1 cc volume of the overlap structure (90% prescribed dose isodose volume). The table also includes the IQR as a measure of data dispersion.

Plan	Median	Minimum	Maximum	IQR
Clinical	4.77	4.59	5.51	0.58
6 directions	4.68	4.45	5.78	0.62
9 directions	4.64	4	6.11	1.04
18 directions	4.69	4.2	6.12	0.37
27 directions	4.66	4.05	6.04	0.92
9 directions, range shifter	4.7	3.93	5.12	0.77
18 directions, range shifter	4.44	3.44	5.48	0.88

Table D.7: Median, minimum and maximum LET$_d$ across all patient population for a 1 cc volume of the overlap structure (90% prescribed dose isodose volume). The table also includes the IQR as a measure of data dispersion.

Plan	Median	Minimum	Maximum	IQR
Clinical	4.42	4.16	4.98	0.53
6 directions	4.28	3.82	5.11	0.53
9 directions	4.12	3.72	5.48	0.57
18 directions	4.18	3.84	5.39	0.32
27 directions	4	3.67	5.27	0.39
9 directions, range shifter	4.24	3.42	4.47	0.59
18 directions, range shifter	4.04	3.25	4.66	0.9

Table D.8: Median, minimum and maximum LET$_d$ across all patient population for a 10 cc volume of the overlap structure (90% prescribed dose isodose volume). The table also includes the IQR as a measure of data dispersion.

Plan	Median	Minimum	Maximum	IQR
Clinical	3.78	3.59	4.16	0.37
6 directions	3.61	3.22	3.91	0.29
9 directions	3.47	3.2	4.56	0.32
18 directions	3.49	3.24	4	0.2
27 directions	3.38	3.17	4.26	0.24
9 directions, range shifter	3.53	3.11	3.76	0.29
18 directions, range shifter	3.42	2.96	3.85	0.44

D.0.2. Tables of the Effective RBE Values for the OARs

Table D.9: Median, minimum and maximum effective RBE values across all patient population (brainstem core). The table also includes the IQR as a measure of data dispersion.

Plan	Median	Minimum	Maximum	IQR
Clinical	1.37	1.21	1.84	0.21
6 directions	1.37	1.18	1.69	0.2
9 directions	1.41	1.09	1.78	0.32
18 directions	1.42	1.13	1.73	0.25
27 directions	1.38	1.11	1.97	0.29
9 directions, range shifter	1.31	1.14	1.69	0.16
18 directions, range shifter	1.33	1.15	1.78	0.13

Table D.10: Median, minimum and maximum effective RBE values across all patient population (brainstem surface). The table also includes the IQR as a measure of data dispersion.

Plan	Median	Minimum	Maximum	IQR
Clinical	1.28	1.16	1.77	0.21
6 directions	1.33	1.13	1.7	0.13
9 directions	1.3	1.14	1.58	0.22
18 directions	1.36	1.1	1.67	0.12
27 directions	1.34	1.15	1.73	0.25
9 directions, range shifter	1.25	1.14	1.77	0.1
18 directions, range shifter	1.25	1.13	1.68	0.09

Table D.11: Median, minimum and maximum effective RBE values across all patient population (optic chiasma). The table also includes the IQR as a measure of data dispersion.

Plan	Median	Minimum	Maximum	IQR
Clinical	1.21	1.16	2.12	0.18
6 directions	1.16	1.05	1.49	0.19
9 directions	1.16	1.12	1.51	0.14
18 directions	1.17	1.14	1.67	0.27
27 directions	1.19	1.11	1.52	0.22
9 directions, range shifter	1.16	1.12	1.52	0.23
18 directions, range shifter	1.17	1.1	1.61	0.25

Table D.12: Median, minimum and maximum effective RBE values across all patient population (left optic nerve). The table also includes the IQR as a measure of data dispersion.

Plan	Median	Minimum	Maximum	IQR
Clinical	1.23	1.16	2	0.29
6 directions	1.22	1.12	1.67	0.18
9 directions	1.19	1.11	1.62	0.17
18 directions	1.17	1.11	1.53	0.15
27 directions	1.22	1.13	1.87	0.14
9 directions, range shifter	1.22	1.11	1.36	0.14
18 directions, range shifter	1.19	1.1	1.37	0.17

Table D.13: Median, minimum and maximum effective RBE values across all patient population (right optic nerve). The table also includes the IQR as a measure of data dispersion.

Plan	Median	Minimum	Maximum	IQR
Clinical	1.34	1.16	2.05	0.42
6 directions	1.33	1.11	1.75	0.23
9 directions	1.26	1.13	1.8	0.11
18 directions	1.3	1.13	1.5	0.16
27 directions	1.24	1.13	1.52	0.15
9 directions, range shifter	1.19	1.1	1.53	0.13
18 directions, range shifter	1.2	1.12	1.56	0.15

E.0.1. Energy Layers per PAT Plan

The total number of energy layers needed for each plan depends on the number of beam directions. In general, more beam directions require additional energy layers. A graph illustrating this data is shown below.
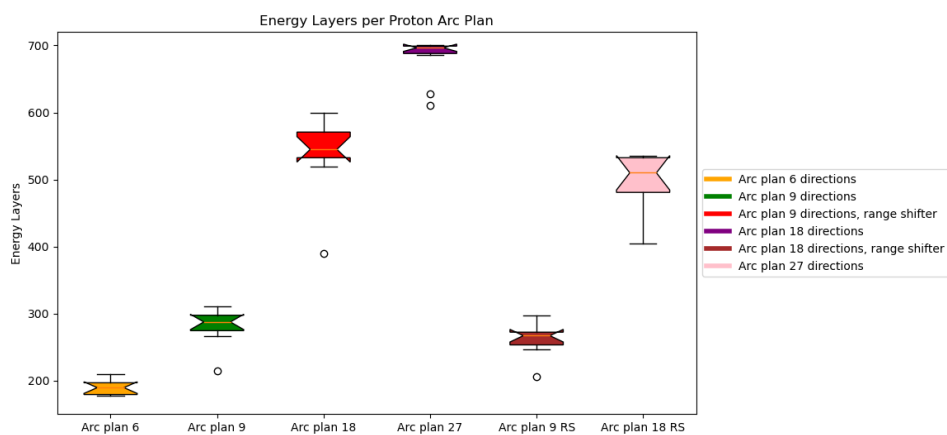
Figure E.1: The amount of energy layers required per plan, across the patient population

Although Figure E.1 indicates that plans utilizing a range shifter require fewer energy layers compared to those without it, subsequent statistical analysis revealed no statistically significant differences. As a result, no definitive conclusions can be drawn from this observation.

E.0.2. Angular Distributions of the Energy Layers, Spots, and MUs for Each Plan of Patient 1
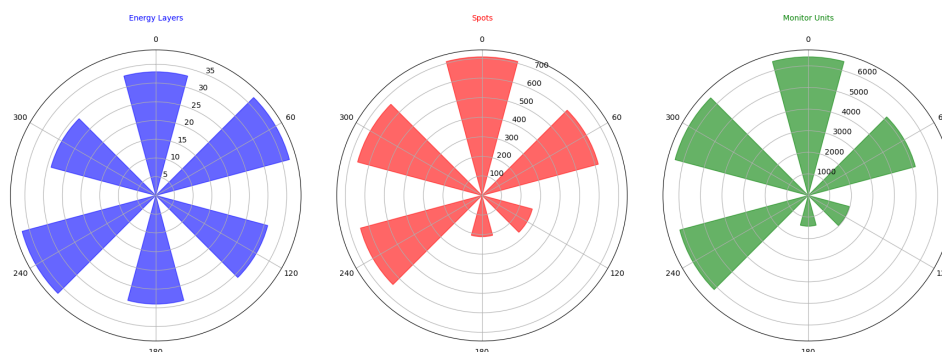
Figure E.2: Angular distributions of the Energy Layers, Spots, and MUs (patient 1, 6-directions plan).
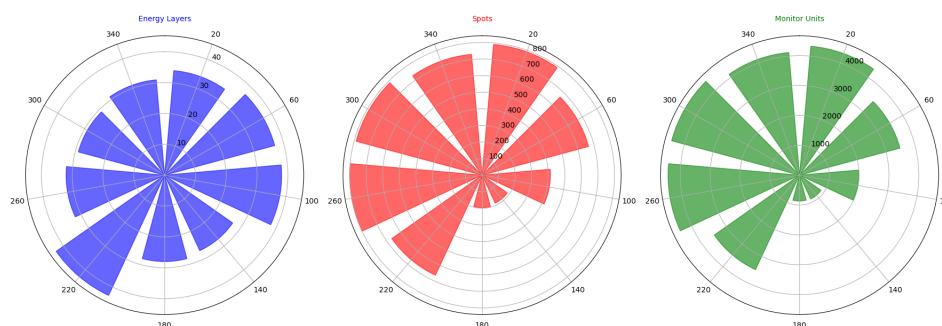
Figure E.3: Angular distributions of the Energy Layers, Spots, and MUs (patient 1, 9-directions plan).
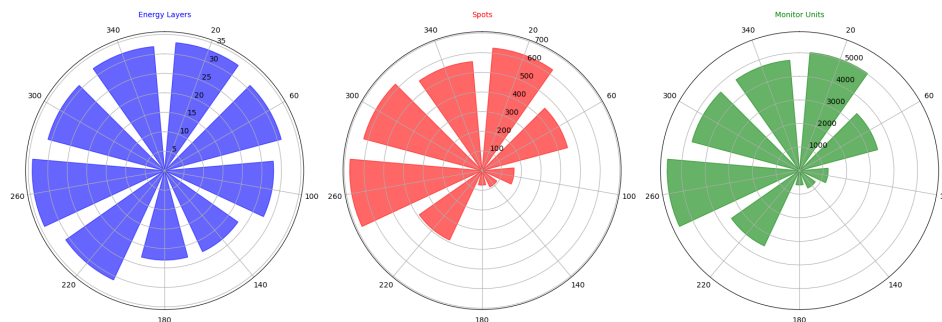
Figure E.4: Angular distributions of the Energy Layers, Spots, and MUs (patient 1, 9-directions plan with range shifter).
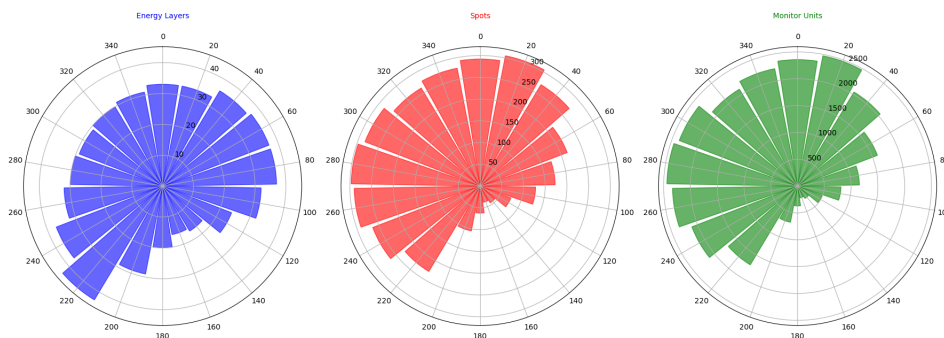
Figure E.5: Angular distributions of the Energy Layers, Spots, and MUs (patient 1, 18-directions plan).
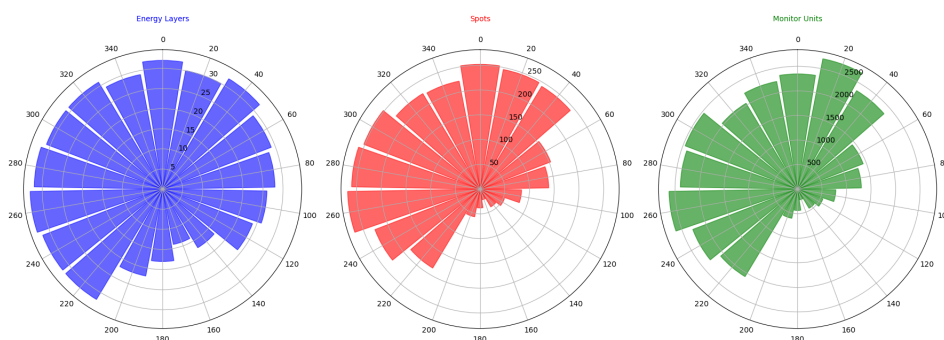
Figure E.6: Angular distributions of the Energy Layers, Spots, and MUs (patient 1, 18-directions plan with range shifter).
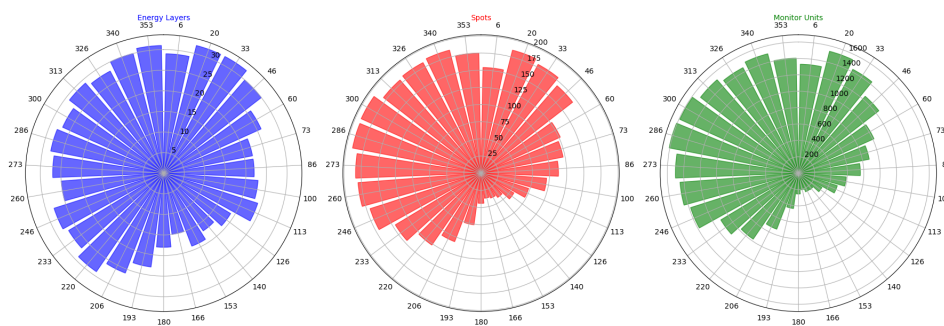
Figure E.7: Angular distributions of the Energy Layers, Spots, and MUs (patient 1, 27-directions plan).

The figures above clearly illustrate that the angular distributions emphasize the location of the CTV region. This is evident from the significantly higher concentration of spots and MUs in this area compared to others. Additionally, the plots reveal that the software does not optimize irrelevant beam directions to better align with the location of the CTV. Instead, it maintains the initial beam configuration established for the entire patient group.

E.0.3. Analysis of the 60% and 90% Isodose Volumes to Assess their Variation with an Increasing Number of Discrete Beam Directions across Different Plans
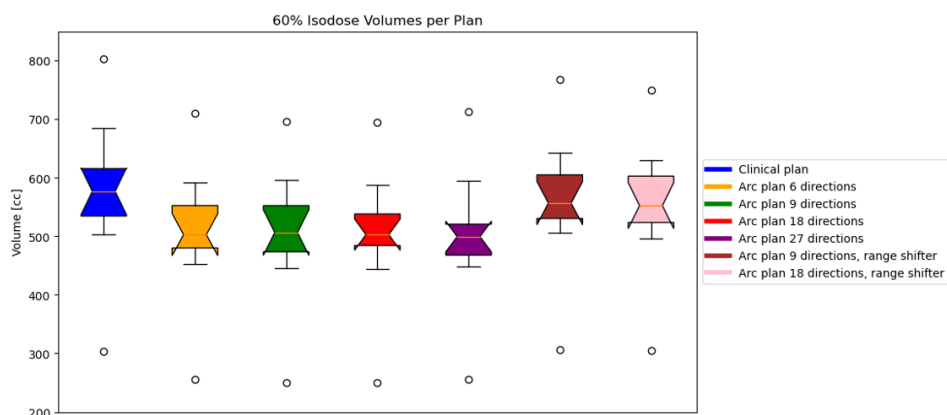
Figure E.8: Boxplots of the 60% isodose volumes per plan.
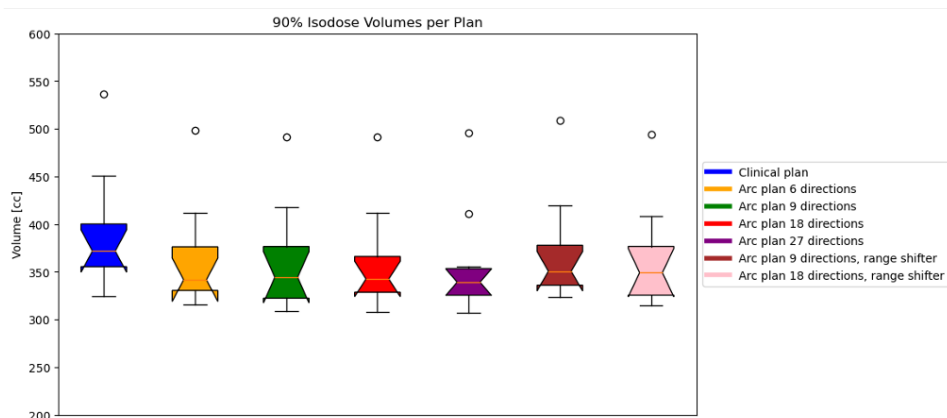
Figure E.9: Boxplots of the 90% isodose volumes per plan.

A statistical analysis using the Shapiro-Wilk test was conducted, which indicated that the isodose volume data for the different plans followed a normal distribution. Following this, an ANOVA test revealed no statistically significant differences, and as a result, no further comparisons can be made.